Babeș-Bolyai University
Faculty of Physics
Doctoral School of Physics

Contributions to the Synthesis and Biomedical Applications of New Noble Metal Nanoclusters and Nanoparticles

Hada Alexandru-Milentie

Scientific Advisor
Prof.dr. Aștilean Simion

Cluj-Napoca
2023

Table of contents

Keywords: gold nanoclusters; noble metal nanoparticles; intrinsic photoluminescence; localized surface plasmon resonance; imaging; sensing.

Motivation and Outline

In an age defined by the imperative for progress, the field of nanotechnology emerges as a guiding light of potential and transformation, particularly in the quest for affordable, efficient, and effective care. Situated at the crossroads of science, engineering, and innovation, nanotechnology embodies unparalleled capacity to confront prevailing global predicaments while addressing the pressing need for accessible healthcare solutions. Operating on the nanoscale – a realm where atoms and molecules collaborate, giving rise to inventive materials and systems – reveals the potential to overhaul industries, from healthcare to energy, from electronics to environmental sustainability. The journey into nanotechnology extends a serious call to stand at the vanguard of change, to channel collective brilliance toward solutions once deemed unattainable. Within a world clamoring for breakthroughs that enrich lives, shield the planet, and provide comprehensive healthcare for all, adopting nanotechnology emerges not solely as a preference, but as an obligation to steer a future harmonized by human resourcefulness, benevolence, and accessible medical advancements.

At the heart of this transformative journey lie noble metal nanoparticles and nanoclusters, exquisite examples of nanotechnology's prowess. These small yet potent structures possess attributes that challenge conventional materials, showcasing extraordinary skill in catalytic reactions, optical phenomena, and antimicrobial behaviors. With the profound potential to redefine medical imaging, sensing technologies, and combatting microbial threats, these little wonders are on their way to reshape the landscape of healthcare applications. Envision precise disease detection mechanisms, sensor systems with unparalleled sensitivity, and novel antimicrobial approaches that mitigate risks – all within reach through the strategic utilization of noble metal nanoparticles and nanoclusters.

The key parameter which defines the properties of this nanomaterials (nanoclusters and nanoparticles) is their size. The effects of size on noble metal nanomaterials' geometric and electronic structure represents one of the most intensively studied matter in this field. It all started from single-atom metal-species with an electronic structure strongly dependent on the surrounding environment (solvent and ligand), whose electronic structure is well defined due to theoretical simulations. However, when it comes to small (nanoclusters) and large (nanoparticles) metal species, their electronic structure becomes a lot more complex. As an example (**Scheme 1**) for gold

(Au) species, the band gap between highest occupied molecular orbital (HOMO) and the lowest unoccupied molecular orbital (LUMO) is highly dependent on the size of Au-species [1]. Specifically, as the size of the nanomaterials increases, the bandgap between HOMO and LUMO decreases until, in the case of nanomaterials with a size surpassing 5 nm, the two orbitals overlap and a continuous energy band form. Due to this size effects, the optical properties of nanomaterials will vary drastically with their size.

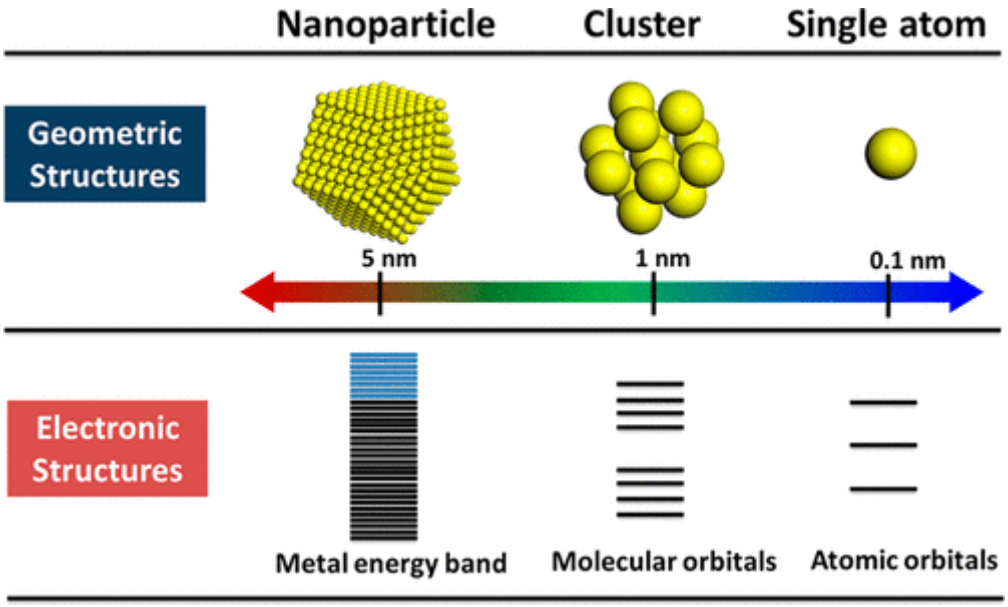

Scheme 1. *Geometric and electronic structure of nanomaterials' dependency on their size. Figure reproduced from* [1].

Therefore, the aim of this work was to deepen the investigation of the physico-chemical properties of both nanoclusters and nanoparticles and to exploit their properties to develop, as a proof-of-concept, new contrast agents, sensing platforms and antimicrobial platforms in order to meet the needs of today's society.

Chapter 1. Overview on noble metal nanoclusters and nanoparticles

1.1. Introduction in nanotechnology

A key parameter which defines the optical properties of NPs is their size, classifying them in (i) plasmonic NPs (above 5 nm) and nanoclusters (NCs - below 5 nm), each of them empowered with different optical properties. When the size of NPs exceeds 5 nm, the NPs present an unique optical phenomenon called localized surface plasmon resonance (LSPR), a collective oscillation of the free electrons from the conduction band after the interaction of the NP with an electromagnetic field (light) [2]. However, if the size decreases below 5 nm, they no longer have the LSPR phenomenon, instead NCs exhibit a tunable intrinsic photoluminescence with excellent photostability and high Stokes shift [3]. Both types of nanoobjects are of high interest nowadays therefore in the following subsections of this chapter, more details about their synthesis, properties and applications are presented.

1.2. Noble metal nanoclusters

1.2.1. Synthesis methods

In the past decade, many new syntheses of NCs were reported, exploiting both the bottom-up and top-down approaches in the search to attain the simplest and the fastest way to achieve NCs with high purity and reproducibility. Among them, the most used is the direct synthesis method also called the one-step synthesis method. Using this approach, the noble metal salt is reduced in the presence of a reducing agent and stabilized by a thiol-based ligand present in abundance in the synthesis solution, resulting in the formation of NCs. However, there are ligands that play both the role of the reducing agent and the stabilizing agent during the synthesis procedure such as proteins [3], peptides [4], amino acids [5], etc, strategy which is also known as template assisted synthesis. The main problem of this procedure is that they are time consuming, taking sometimes even days to obtain NCs, which was the case of bovine serum albumin encapsulated NCs synthesized also in this work.

The microwave-assisted approach can considerably reduce the synthesis time to even minutes. This approach comes with many other advantages such as uniform heating, a low energy consumption resulting in excellent cost effectiveness, while being eco-friendly [6,7]. Moreover,

the procedure exhibits a high control on the dispersity of the synthesized nanocrystals. This strategy was used in the work presented in this thesis to successfully synthesize NCs stabilized by glutathione and histidine.

1.2.2. Properties of nanoclusters

The property of NCs which attracted extensive attention is their intrinsic photoluminescence. The emission of NCs can be affected by various factors from the structure of the NCs to the solution pH or temperature [8]. Up until now, the emission mechanism is unknown to the research community. Yet, the quantum confinement effect is accepted. Specifically, bulk materials present a continuous energy band, however, when the size of the nanomaterial becomes comparable to the Fermi wavelength (~ 2 nm), the continuous energy band splits into discrete energy levels [9], empowering NCs with molecular-like properties such as photoluminescence.

1.2.3. Applications of nanoclusters

Due to their unique physicochemical properties such as biocompatibility, excellent bio-permeability and easy-to-modify surface, NCs are extensively being exploited in various applications. Among them, NCs are exploited the most as sensing platforms as their photoluminescence is highly sensitive. After the interaction with the desired analyte, usually, the intensity of photoluminescence varies in two possible ways: (i) quenching and (ii) emission enhancing Cell and tissue imaging is another application in which NCs are extremely exploited. Due to their small size (1-5 nm), NCs can easily penetrate the cell membrane, while exhibiting high chemical- and photo- stability, high biocompatibility given by the stabilizing agent making them excellent candidates as fluorescent contrast agents for bioimaging applications. Even though the aforementioned applications are the most exploited, great works were reported with NCs even in other fields. In the work which will be presented in this thesis, the synthesized NCs will be exploited in their two main applications: sensing and imaging.

1.3. Noble metal nanoparticles

1.3.1. Synthesis methods

The synthesis of NPs as the one of NCs can be achieved following one of the two main strategies: the bottom-up approach and the top-down one. The top-down approaches imply breaking the bulk material into small NPs *via* a physical or chemical method. For this approach, there are multiple strategies reported in the literature such as pyrolysis, thermolysis, nanolithography and radiation-induced approaches. However, most of the top-down strategies result in the formation of NPs with surface imperfections affecting their both physical and chemical properties. The NPs produced by bottom-up strategies are in general considered of higher quality due to the possibility to control their composition, size and shape. The bottom-up approaches are usually aqueous-chemical synthesis such as chemical, sonochemical, electrochemical and green approaches. The reduction of metal ions in solution represents the most exploited bottom-up strategy and implies the reduction of noble metal ions from their corresponding salts using different chemical compounds as reducing agents in the presence of suitable stabilizing agent [10]. Moreover, the green strategies involve the use of microorganism, biopolymers and plant extracts to be used as stabilizing agents and sometimes even reducing agents [11]. In this work, the green synthesis strategy was the only one exploited to synthesize NPs.

1.3.2. Properties of nanoparticles

In order to understand the physical meaning of surface plasmons, metallic NPs should be approximated as a network of positive ions inside which electron from the conduction band are freely moving [2]. After the interaction of NPs with light, the electromagnetic field exerts a force on the freely moving electrons which push them towards the surface of the NPs. The movement of the conduction electrons will result into a charge separation which will create an electric dipole. At this point, the electric dipole will generate and opposite electric field which will compel the electrons to return at their equilibrium point. Therefore, the conductive electrons will start oscillating around their equilibrium point with a frequency also known as the plasmonic frequency. The oscillation of electrons from the conductive band after their excitation with light bears the name of surface plasmons [12]. Moreover, if the frequency of the electromagnetic field matches the plasmonic frequency, the conduction electrons will oscillate at maximum amplitude resulting

in the most important phenomenon of NPs, surface plasmon resonance. In addition, if the NPs are made out of metal, surface plasmon resonance is localized on the surface of the NPs which represents the phenomenon known as LSPR.

1.3.3. Applications of nanoparticles

Due to their unique physical and chemical properties, noble metal NPs were exploited in various applications. Among all, NPs were extensively used in sensing to selectively detect the desired analyte. Most of the reported sensing strategies involving NPs are based on their aggregation after interacting with the target molecule, resulting in a change in color of their colloidal solution, called colorimetric detection. Imaging is another application in which noble metal NPs perform well. Even though NPs can play the role of contrast agents by themselves for dark-field imaging [13], however this technique implies high-intensity light to excite the NPs-treated cells or tissue which can cause damage to them. Therefore, NPs are functionalized with a Raman reporter molecule or a fluorophore to play the role of contrast agents for surface enhanced Raman scattering (SERS) imaging [14] or fluorescence imaging [15], respectively. In the work presented in this thesis, the synthesized NPs were exploited as colorimetric sensing platforms, SERS contrast agents and antimicrobial agents.

Taking in consideration the different optical properties between NCs and NPs, in the following, the thesis will be split into two parts (I) “Contributions on the synthesis of new gold nanoclusters and their applications in bioimaging and sensing” focusing on the synthesis, characterization and imaging and sensing applications of NCs and (II) “Contributions on the synthesis of new noble metal nanoparticles for applications as SERS contrast agents, nanoantibiotics and sensing platforms “ focusing on the synthesis, characterization and imaging and sensing applications of NPs.

Part I. Contributions on the synthesis of new gold nanoclusters and their applications in bioimaging and sensing

Chapter 2. Bovine serum albumin stabilized gold nanoclusters for fluorescence lifetime imaging applications

2.1. Introduction

In the past decades, fluorescence imaging has been proven to be a powerful technique for the early diagnosis and treatment guidance of diseases, but also crucial in mechanism studies of different biological, immunological and neurological processes [16–21]. Therefore, the development of adequate fluorescent contrast agents has become a priority for the research community [22,23]. Usually, a fluorescent contrast agent is composed of a visible or near-infrared (NIR) emitting fluorophore functionalized with a biomarker that exhibits high affinity for a receptor from the cell or tissue of interest. However, common organic fluorophores present multiple disadvantages like overlapped emission with the biological autofluorescence, fast fluorescence lifetimes, low photostability, a small Stokes shift, but can also be highly toxic for the biological environments [24,25]. Therefore, it is crucial to fabricate fluorescent contrast agents that are able to overcome the aforementioned drawbacks.

2.2. Synthesis of BSA-AuNCs

BSA-AuNCs were synthesized using an adapted and optimized two-step procedure, that was previously reported [3]. In an Erlenmeyer flask, 5 mL solution of BSA (40 mg/mL) were mixed with 5 mL of $HAuCl_4$ (10^{-2} M) under magnetic stirring at 37 ℃. Forward, 20 µL of ascorbic acid (10^{-3} M) and 0.5 mL of NaOH (1 M) were dropped at a rate of 4 µL/min and 0.1 mL/min, respectively. After 24 h, 0.5 mL of NaOH (1 M) were added to adjust the pH of the solution to a very alkaline one and the solution was magnetically stirred for another 24 h at 37 ℃.

2.3. Characterization of BSA-AuNCs

Following the synthesis, the colloidal solution of BSA-AuNCs exhibits a dark-brown color under ambiental light (**inset - Figure 2.1.A**) which turns red when exposed to ultraviolet light, indicating that the synthesized particles possess intrinsic photoluminescence. Moreover, the colloidal solution of BSA-AuNCs presents a strong absorption that exponentially decreases from UV to visible (**Figure 2.1.A**), while the absence of a localized surface plasmon resonance band (LSPR) demonstrates the absence of large nanoparticles.

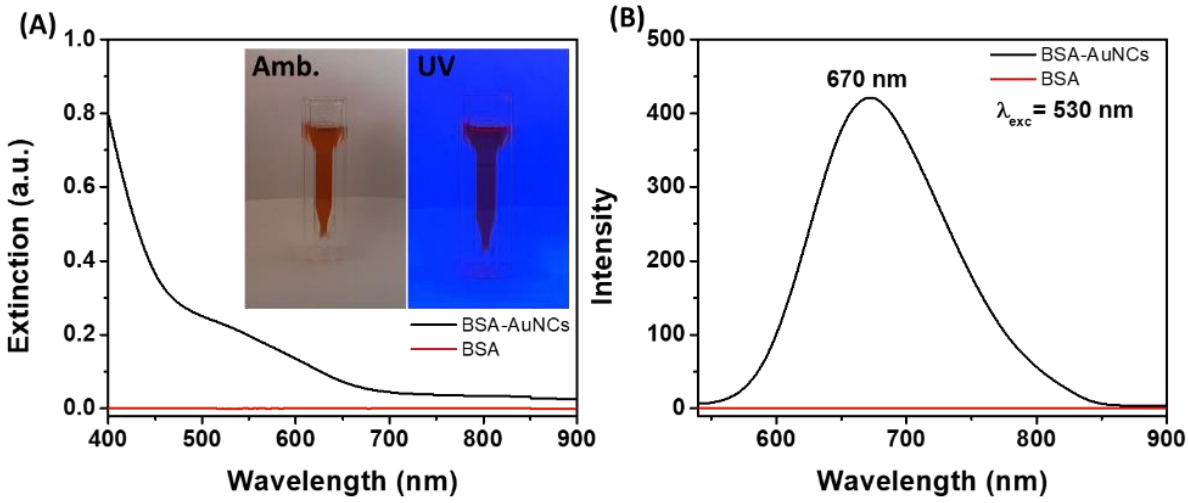

Figure 2.1. *(A) The absorption and (B) the photoluminescence spectra of BSA-AuNCs (black line) and BSA (red line). The inset represents the colloidal solution of BSA-AuNCs exposed to ambiental light and UV light. Figure adapted from* [26].

From the emission point of view, the colloidal solution of BSA-AuNCs exhibits a far-red photoluminescence localized at 670 nm under 530 nm excitation (**Figure 2.1. B**). It is worth mentioning that no emission was observed from an equivalent solution of BSA under the same excitation wavelength. From the morphological point of view, the DLS measurements (**Figure 2.3.A**) present that the average size of the BSA-AuNCs is 25 ± 12 nm. Taking in consideration that a single BSA protein possesses dimensions of 4 nm x 4 nm x 14 nm, the reported hydrodynamic size of BSA-AuNCs indicates the polymerization of multiple BSA chains. This theory was confirmed by low magnifications TEM images that are presented in **Figure 2.3.B**. Furthermore, the HRTEM images of an BSA-AuNCs complex (**Figure 2.3.C**) demonstrate the presence of 2 to 3 nm spherical nanostructures inside the BSA complex, while the EDX elemental analysis clearly confirms the nanostructures are made out of gold. Therefore, the DLS and TEM measurements proves the successful synthesis of AuNCs wrapped inside a BSA corona.

2.3. Folic acid functionalization of BSA-AuNCs

The ovarian adenocarcinoma cells overexpress the folate receptor alpha (FRα), while the receptor is barely found in normal healthy cells and, therefore, the functionalization with FA would

empower BSA-AuNCs with targetability towards ovarian cancer cells. After performing the procedure detailed in subsection 2.2.3, the functionalization with FA of BSA-AuNCs was first evaluated using the FT-IR spectroscopy and a new C-N covalent was observed between the carboxyl group of FA and the amine group of BSA. The hydrodynamic size of BSA-AuNCs increases by 3 nm after the FA-functionalization, while an increase in value by 10 mV of the zeta potential post-functionalization was observed. Furthermore, the photoluminescence of BSA-AuNCs before and after the FA-functionalization was investigated under 530 nm excitation and the BSA-specific emission band presented a 12 nm blue shift and a slight decrease in intensity post-functionalization with FA. All the aforementioned results prove that the BSA-AuNCs were successfully functionalized with FA.

2.4. Cell viability of BSA-AuNCs

In order to develop AuNCs for biomedical applications, the key property they should possess is biocompatibility. Therefore, the viability of ovarian adenocarcinoma NIH:OVCAR-3 cells, a cell line with overexpressed FRα on their surface, was tested in the presence of BSA-AuNCs and FA-BSA-AuNCs. Both samples don't exhibit any toxic effects on the viability of the NIH:OVCAR-3 cell line at any tested concentration, demonstrating their high biocompatibility.

2.5. Performance of BSA-AuNCs as fluorescence contrast agents

2.5.1. Inside cells

We evaluated the potential of BSA-AuNCs as photoluminescent contrast agents for the targeted visualization of ovarian adenocarcinoma NIH-OVCAR-3 cells using a fluorescene lifetime imaging microscopy (FLIM - **Figure 2.2.**) under 520 nm excitation. The photoluminescence lifetime maps of the untreated and AuNCs-treated NIH:OVCAR-3 cells demonstrates the enhanced cellular uptake of FA-BSA-AuNCs compared to BSA-AuNCs, uptake-superiority which is mediated by FA. The AuNCs are preferably located around the nucleus, highlighting the cellular cytoplasm, while no signal was depicted from the untreated cells under the same 520 nm excitation. Moreover, the high-contrast FLIM images acquired on the FA-BSA-AuNCs treated NIH-OVCAR-3 cells at different z-depths confirm the uniform distribution of the AuNCs inside the whole cell (**Figure 2.17.z1-5**).

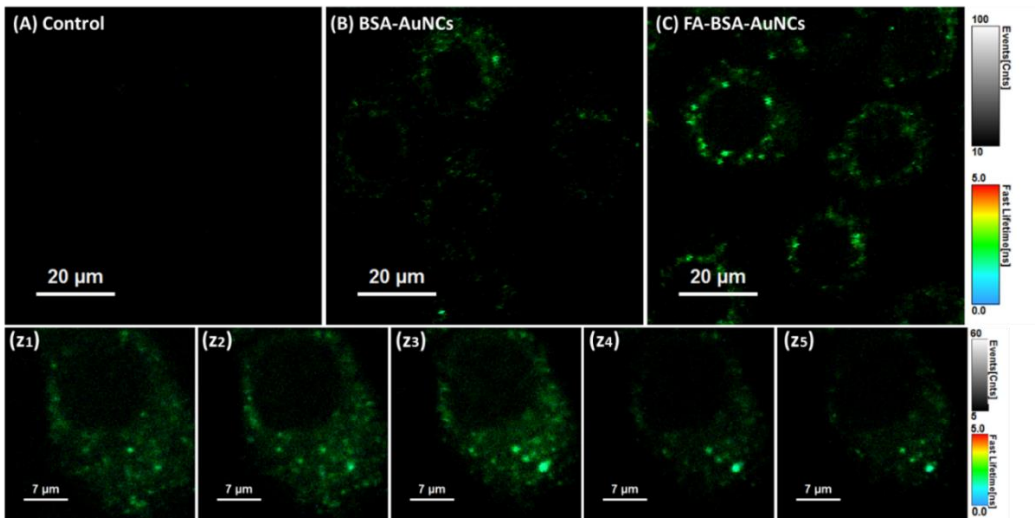

Figure 2.2. *High-contrast confocal FLIM images of untreated ovarian adenocarcinoma NIH:OVCAR-3 cells, (B) treated with BSA-AuNCs and (C) with FA-BSA-AuNCs. ($z_{1\text{-}5}$) FLIM images of the same FA-BSA-AuNCS-treated NIH:OVCAR-3 cell recorded at different z-depths. All images were acquired under 520 pulsed one-photon excitation. Figure reproduced from* [26].

Therefore, the aforementioned results demonstrate the excellent cellular-staining effect of FA-BSA-AuNCs together with their uniform internalization and, in consequence, their capacity to be used as cancer-specific photoluminescent contrast agents for intracellular bioimaging.

2.5.2. Inside tissue-mimicking phantoms

Unfortunately, most imaging studies stop at the cellular levels, however, further studies need to be performed on more complex biological environments in order to assess the feasibility of a nanomaterial to be used as a contrast agent. Therefore, BSA-AuNCs at different concentrations were internalized in agarose-phantoms (BSA-AuNCs@phantom) and their efficiency as photoluminescent contrast agents was evaluated under NIR TPE. The acquired TPE FLIM images are presented in **Figure 2.3**. The FLIM images of the agarose-phantoms treated with 20-50% BSA-AuNCs (20-50%BSA-AuNCs@agarose-phantom) recorded under 820 nm TPE exhibit a homogeneous photoluminescence, while no signal was detected from the untreated agarose-phantom (control). Specifically, the precise delimitation of the phantom regions that were treated with BSA-AuNCs from the untreated ones demonstrates their ability to stain tissue mimicking agarose-phantoms under non-invasive NIR TPE.

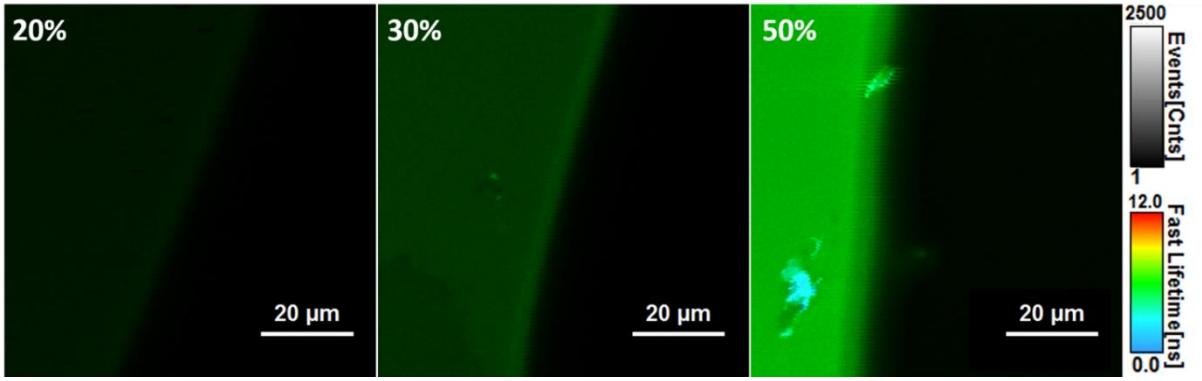

Figure 2.19. *FLIM images of agarose-phantoms treated with different concentrations of BSA-AuNCs (20, 30 and 50%) acquired under 820 nm TPE. The FLIM maps are represented in the same lifetime (0-12 ns) and intensity scale (0-2500 counts). Image reproduced from* [27].

Furthermore, even though the photoluminescence intensity increases with the concentration of BSA-AuNCs, inside the agarose-phantom treated with 50% BSA-AuNCs high-aggregation regions were found. These regions can be depicted as the light-blue spots due to a lower photoluminescence lifetime value. Taking in consideration that aggregated NCs and proteins present high toxicity to any cell or tissue, the agarose-phantom treated with 30% BSA-AuNCs was chosen to be used in the following experiments.

High depth penetration, reduced phototoxicity, highly localized excitation represent just some of the advantages of TPE over OPE. While for OPE, a linear dependency can be observed between the emission intensity and the power of the excitation, for TPE a non-linear dependency should be observed. Therefore, the photoluminescence spectrum from the AuNCs-treated phantom was extracted for different between 5 and 20 mW. First, the optical information of the 30%BSA-AuNCs@agarose-phantom's photoluminescence matches the one of BSA-AuNCs in solution and solid-state with a maximum localized at 670 nm, proving that their emission properties are maintained inside the agarose-phantom. Secondly, the photoluminescence intensity quadratically depends on the used excitation power, demonstrating without a doubt that the emission is the result of a TPE process. Therefore, BSA-AuNCs represent excellent candidates as reliable photoluminescent contrast agents for future non-invasive *in vivo* TPE-FLIM imaging applications.

2.6. Conclusions

In this chapter, BSA-stabilized AuNCs showed an excellent performance as photoluminescent contrast agents for both intracellular-targeted imaging and simulated *ex vivo* imaging inside tissue mimicking agarose-phantom *via* FLIM under one-photon and two-photon, respectively, excitation. After the two-step synthesis, the colloidal solution of BSA-AuNCs exhibited a bright red emission localized at 670 nm under 530 nm excitation that is stable in time, in different states of matter and also under continuous irradiation. Furthermore, the BSA-AuNCs were successfully functionalized with FA and their excellent biocompatibility was proved by MTT assays performed on ovarian adenocarcinoma NIH:OVCAR-3 cells. Next as a proof of concept, *in vitro* fluorescence microscopy imaging demonstrated the excellent intracellular-staining ability of BSA-AuNCs, but also that the FA-functionalization significantly improved their internalization inside ovarian adenocarcinoma NIH:OVCAR-3 cells. Finally, the BSA-AuNCs were internalized inside tissue mimicking agarose-phantoms, as a bioethical step before *in vivo*, in order to evaluate their bioimaging abilities in a simulated *ex vivo* environment. An outstanding signal was obtained in the case of the 30%BSA-AuNCs@agarose-phantom under 820 nm TPE, while the quadratic dependency of the signal on the excitation power confirmed that the photoluminescence originates from a TPE process. Therefore, BSA-AuNCs represent promising candidates for future targeted non-invasive *in vivo* imaging.

Chapter 3. Glutathione-capped gold nanoclusters as near-infrared-light emitters for confocal fluorescence imaging

3.1. Introduction

NIR-emitting contrast agents represent a class of biocompatible and fluorescent nanomaterials that were proven to be excellent tools for non-invasive deep-tissue imaging. Exhibiting both excitation and emission maximum wavelengths in the first biological window, NIR-emitting contrast agents can be tracked inside tissue up to a depth of 1 cm, making them excellent candidates for *in vivo* imaging applications [28]. Up to today, some NIR-emitting FDA-approved fluorophores were already exploited for live fluorescence-based surgical guidance [29,30], however, they present significant drawbacks like low temporal stability, low Stokes shift and a fluorescence lifetime that overlaps with the one of tissue's autofluorescence. Therefore, the development of new NIR-emitting biocompatible contrast agents to overcome the aforementioned drawbacks is necessary and critical for the evolution of fluorescence-based image-guided surgery.

3.2. Synthesis of GSH-AuNCs

Multiple types of GSH-AuNCs were synthesized *via* a new microwave-assisted procedure which is presented in **Scheme 3.1**.

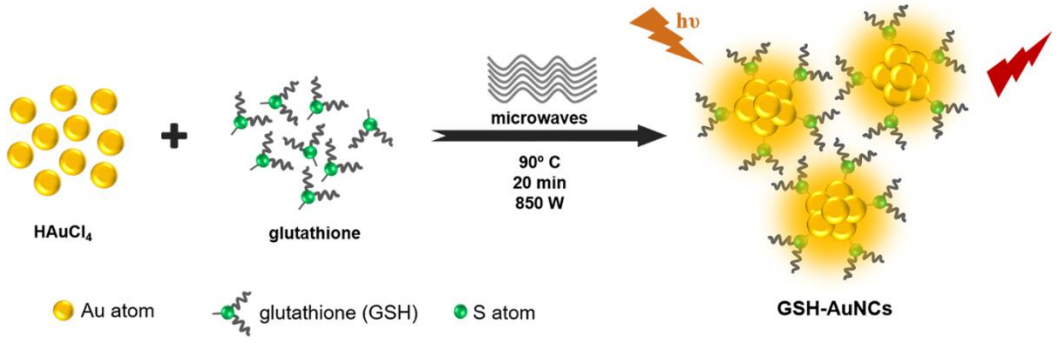

Scheme 3.1. Schematic representations of the microwave-assisted synthesis of GSH-AuNCs

In a G10 microwave-reactor's vessel, a solution of GSH (3 mL, 5 mM) was added over volumes ranging between 1.0 and 1.3 mL of $HAuCl_4$ (10 mM). Afterwards, the vessels were irradiated by 850 W microwaves for 20 min at 90 °C.

3.3. Characterization of GSH-AuNCs

First of all, multiple batches of GSH-AuNCs were synthesized using the procedure presented in **Scheme 3.1** by ranging the $HAuCl_4$ between from 1.0 to 1.3 mL. Compared to other reported procedures, the novelty of the approach presented in this chapter consists of the use of microwave irradiation for the controlled reduction of gold ions, synthesis times which are considerably faster (20 min) and the high control of their optical properties by changing the GSH:$HAuCl_4$ molar ratio, resulting in a green, fast and simple procedure. All the batches of GSH-AuNCs present two fluorescence emissions bands under 405 nm excitation: a photoluminescence localized at 610 nm (red-PL) and one located at 800 nm (NIR-PL). The dual photoluminescence of GSH-AuNCs is due to the two different conformations that GSH exist on the AuNCs' surface together with a different surface-coverage degree that GSH ensures [31]

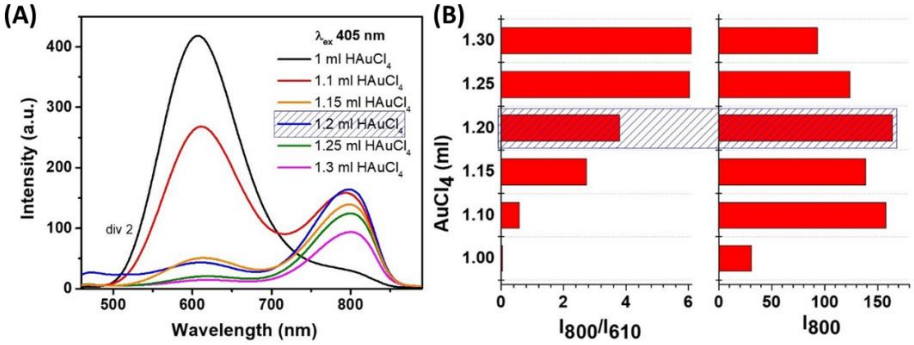

Figure 3.1. *The photoluminescence spectra of all the batches of GSH-AuNCs synthesized by ranging the volume of $HAuCl_4$ from 1.0 to 1.3 mL under 405 nm excitation. (B) The dependence of the photoluminescence intensity ratio (I_{800}/I_{610}) along with the emission intensity of the 800 nm photoluminescence on the used volume of $HAuCl_4$. Figure reproduced from* [32].

Taking in consideration that this chapter is focused on the synthesis of NIR-emitting photoluminescent contrast agents, after a careful analysis of the intensity ration between the red and NIR emissions correlated with the NIR-PL intensity (**Figure 3.1.B**), the GSH-AuNCs synthesized with 1.2 mL of $HAuCl_4$ were chosen for further investigations.

The selected GSH-AuNCs exhibit an absorption behavior typical to NCs with a high absorption in the UV region that rapidly decreases towards the visible region. The GSH-AuNCs colloidal solution presents a green-yellowish color which turns red under UV exposure, a visual confirmation of their intrinsic photoluminescence. The excitation spectrum highlights the wide range of wavelengths at which the NIR-PL can be obtained. The QY of the NIR-PL of GSH-

AuNCs was calculated relatively to indocyanine green and is found to be 9.9%. Moreover, the fluorescence lifetime of the red-PL was measured to be 407 ns, while the one of the NIR-PL was obtained to be 1821 ns, both exhibiting values above the one the biological autoflorescence, proving their feasibility to be used as photoluminescent contrast agents.

3.4. Performance of GSH-AuNCs as near-infrared contrast agents inside tissue-mimicking phantoms

Taking in consideration that the high biocompatibility of GSH-AuNCs was previously reported in multiple studies, the microwaved-synthesized GSH-AuNCs were internalized inside tissue mimicking agarose-phantoms in order to evaluate their efficiency as NIR-emitting contrast agents using complementary re-scan confocal fluorescence microscopy (RCM) and FLIM techniques under 640 nm excitation. The FLIM images of the GSH-AuNCS@agarose-phantom exhibits large spots of high intensity photoluminescent-signal under excitation at 640 nm (**Figure 3.2**), while no signal was depicted from the untreated agarose-phantom (control), demonstrating the recorded signal originates from the photoluminescent NIR-emitting GSH-AuNCs that were embedded inside the agarose-phantom. Moreover, the photoluminescence spectrum acquired from the GSH-AuNCs@agarose-phantom under 640 nm exhibit a 25 nm blue-shift compared to the one in solution and in solid-state. This shift was most probably caused by the agglomeration of the NCs that takes place after internalizing GSH-AuNCs inside the tissue mimicking agarose-phantom. Last but not the least, the 3D-RCM images of the GSH-AuNCs@agarose-phantom, obtained after the reconstruction of multiple confocal 2D images from different z-depths, confirm the distribution of GSH-AuNCs inside the whole mass of the tissue mimicking agarose-phantom, which are in direct agreement with the aforementioned FLIM images. Considering that most of the photoluminescent contrast agents are tested only on cells, in this chapter, it was demonstrated that NIR-emitting long-lived GSH-AuNCs are able to perform as bright and reliable photoluminescent contrast agents inside tissue mimicking agarose-phantoms and, therefore, demonstrating their potential to be used in future *ex vivo* and even *in vivo* bioimaging applications *via* both confocal steady-state fluorescence microscopy and fluorescence lifetime imaging microscopy.

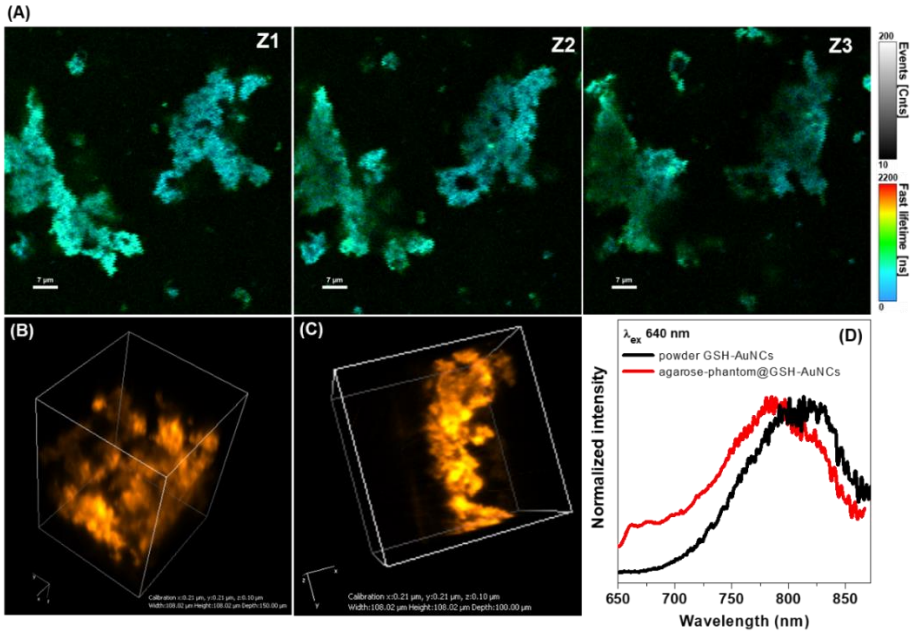

Figure 3.2. *FLIM images of the tissue mimicking agarose-phantom treated with GSH-AuNCs recorded at different z-depts (Z_1-Z_3) under 640 nm excitation with 647LP emission filter. (B) and (C) RCM images of tissue mimicking agarose-phantom treated with GSH-AuNCs acquired under 640 nm excitation. (D) The photoluminescence spectra of GSH-AuNCs in solid state compared to the one recorded inside the tissue mimicking agarose-phantom. Figure reproduced from* [32].

3.5. Conclusions

In this chapter, dual-emissive GSH-AuNCs were synthesized using a novel procedure and was proved to have the capacity to perform as NIR-emitting contrast agents inside tissue mimicking agarose-phantoms using confocal steady-stated fluorescence and lifetime imaging microscopies. In particular, photoluminescent and photostable GSH-AuNCs were synthesized through a microwave assisted approach. The as prepared NCs exhibit two emissions: the red-PL located at 610 nm and the NIR-PL localized at 800 nm with an QY of 9.9%. The fluorescence lifetime of GSH-AuNCs' two emissions were found to be 407 ns for the red-PL and 1821 for the NIR-PL. Furthermore, GSH-AuNCs were proved to exhibit a photostable, bright and uniform NIR-PL under an excitation of 640 nm making them suitable for bioimaging applications. Therefore, complementary RCM and FLIM assays were executed on agarose-phantoms treated with GSH-AuNCs and the obtained images demonstrated the excellent staining capacity of the novel material proposed in this chapter inside tissue-like environment.

Chapter 4. Paper-based portable platforms using as synthesized gold nanoclusters for efficient heavy metal ions detection

4.1. Introduction

In past decades, heavy metal ion pollution has been found to be a major source of concern for the environment and human health because of its high toxicity and non-biodegradable properties [33–35]. For example, high concentration of copper ions (Cu^{2+}) can cause liver or kidney failure [36], but can be also deadly for the subaquatic life [37], while Fe ion can induce disorders such as Parkinson, Alzheimer or even low blood pressure [38]. Nowadays, multiple ways are used to determine the concentration of heavy metal ions from water samples such as atomic absorption spectroscopy [39], surface enhanced Raman spectroscopy [40], chromatography [41], electrochemical methods [42] and even inductively coupled plasma mass spectroscopy [43]. However, the aforementioned sensing techniques have the same drawback: expensive and time-consuming as the samples need to be sent to specialized laboratories or institutions where trained personnel perform the analysis using heavy and expensive equipment. Therefore, there is a big call to develop new, faster and more accessible methods to sensitively and selectively detect the desired heavy metal ion.

4.2. Bovine serum albumin stabilized gold nanoclusters for selective and sensitive Cu ions detection

4.2.1. Synthesis of BSA-AuNCs

The BSA-AuNCs were synthesized using a similar procedure described in subsection 2.2.2. In detail, the temperature of the synthesis was increased to 50 °C, which improved the time of the procedure by 24 h. Moreover, the addition of NaOH (0.5 ml, 1 M) for the second time was not necessary anymore, as the synthesis was completed after only 24 h.

4.2.2. Characterization of BSA-AuNCs

After, the synthesis of BSA-AuNCs,, the NCs were characterized both spectroscopically and morphologically. The UV-Vis spectrum presents a typical NCs absorption, while no localized surface plasmon resonance band could be depicted in the visible region. Moreover, the emission of the BSA-AuNCs was evaluated using a portable spectrofluorometer equipped with LED-based

excitation. The photoluminescence of BSA-AuNCs display a peak located at 670 nm under 502 nm excitation, the most suitable LED in order to maximize the photo luminesce emission. Furthermore, the HR-TEM images, acquired using a Hitachi microscope, expose the AuNCs with an average size of 3 nm which are embedded inside a BSA-corona. Both spectroscopical and morphological characterization demonstrate the successful formation of BSA-AuNCs.

4.2.3. Performance of BSA-AuNCs-based colloidal sensor

The sensitivity and selectivity assays were performed using a light-weight, portable and cheap set-up that can be taken directly to the prelevation site and quantify the desired analyte. After the interaction of BSA-AuNCs with different common metal ions, a 53% quenching of their photoluminescence was observed after interaction with Cu ions, proving their selectivity towards the detection of Cu ions. Next, the colloidal sensor' sensitivity towards the detection of Cu ions was evaluated in solution. Therefore, the colloidal solution of BSA-AuNCs was incubated with Cu^{2+} solutions, and an increasing quenching was obtained with the increase of the tested Cu concentration (**Figure 4.1.A**)

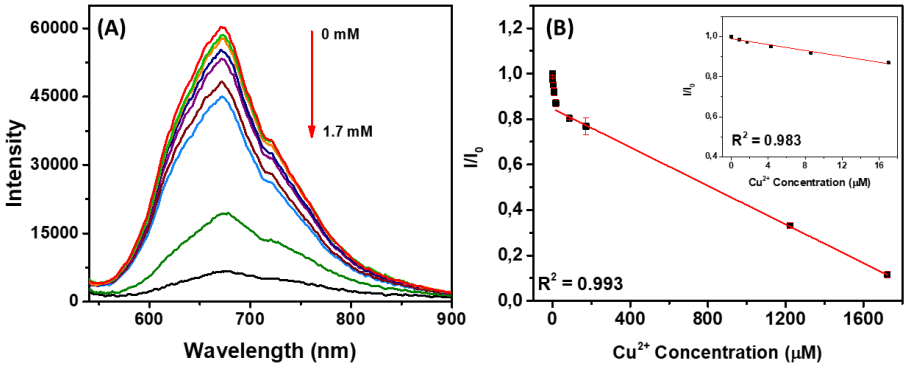

Figure 4.1. *(A) The photoluminescence spectra of BSA-AuNCs under 502 nm excitation in the presence of Cu^{2+} concentrations (B) The sensitivity assay presented as the photoluminescence of BSA-AuNCs' intensity ratio (I/I_0) dependence on the Cu^{2+} concentration. Figure adapted from* [44].

After linear fitting operations performed on the plot of I/I_0 against the Cu^{2+} concentration (**Figure 4.1.B**), two linear dynamic ranges were observed: one for a lower concentration range (0-17 μM) and one for higher concentration range (17-1724 μM). Furthermore, the limit of detection of the colloidal sensor was calculated to be 0.83 μM, a value that is far below the accepted limit in

drinking water of 20 μM set by the USA's Environmental Protection Agency, proving the feasibility of the proposed sensor towards the quantification of harmful concentrations of Cu ions.

4.2.4. Cu ions sensing using BSA-AuNCs-paper-based platform

4.2.4.1. In laboratory conditions

Nowadays, the development of new, cheap and easy-to-use detection methods that can overcome the drawbacks of complicated and time-consuming approaches represent the number one goal of the sensing-niche. Therefore, as a proof of concept, the excellent properties of filter paper were combined with the sensing capacity of BSA-AuNCs in order to develop a cheap, portable, qualitative and semi-quantitative sensor for the specific detection of Cu ions. In particular, concentration ranging from 0 to 250 μM of Cu ions were dropped over the round-shaped BSA-AuNCs-embedded paper spots and the photoluminescence's quenching effect was evaluated (**Figure 4.2)**.

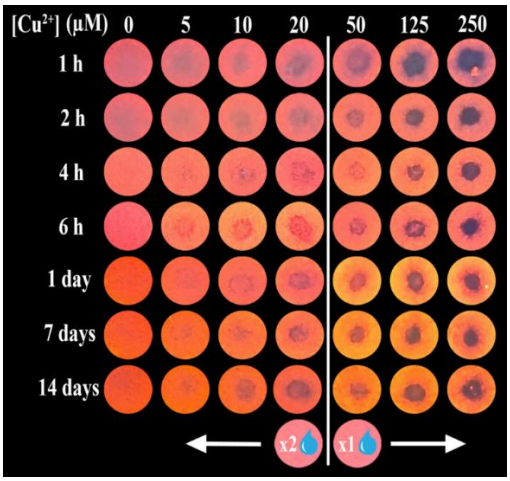

Figure 4.2. *Photographic images of the BSA-AuNCs@paper-based sensor acquired under UV light, 1 h after the incubation with Cu ions at concentrations ranging from 0 to 250 μM. The BSA-AuNCs-embedded paper spots were priorly left to dry for different periods of time ranging from 1 h to 14 days. Figure reproduced from* [45].

Compared to the control-spots incubated with only ultrapure water (the left column of **Figure 4.2**), color alterations were depicted in the middle of the detection spots which were incubated with a Cu^{2+}-containing solution. This phenomenon occurs due to the quenching effect of the BSA-AuNCs' photoluminescence activated by their interaction with Cu ions inside the filter

paper. The different behavior of the paper-based sensor over two concentration ranges (from 5 to 20 μM and over 50 μM) is consistent with the two linear dynamic ranges obtained in the case of the colloidal sensor. The limit of detection of the BSA-AuNCs@paper-based sensor was found to be 5 μM.

4.2.4.2. From real water samples

The next step was to evaluate the BSA-AuNCs@paper-based sensor capacity to detect Cu ions from real water samples. The real water samples exhibited no detectable levels of Cu ions. Therefore, the samples were spiked with 5, 10, 20, 157 and 188 μM, respectively, and assays were carried on. The visual examination of the photos demonstrates that the BSA-AuNCs@paper-based sensing platform is capable to detect concentration as low as 5 μM from real water samples. Even though this concentration is harmless for the human body, it can kill fish after exposure for just a few hours [46].

4.2.5. Conclusions

In conclusion. the BSA-AuNCs@paper-based sensing platform can be successfully used in one of two ways: (1) when exploited for drinking water assays, the quenching produced by a 5 μL drop of water indicates that it contains concentrations exceeding 50 μM of Cu ions and (2) when exploited for the subaquatic environment, the visual detection of Cu after two 5 μL drops confirm that the water sample is deadly for the fish and any other subaquatic life. Therefore, the BSA-AuNCs@paper-based sensor presents great promise for the easy, fast and cheap detection of Cu^{2+} from real waters samples.

4.3. Histidine-capped gold nanoclusters for selective and sensitive Fe ions detection

4.3.1. Synthesis of His-AuNCs

In this work, we developed a new procedure to synthesize His-AuNCs *via* a microwave assisted-approach. In a G10 microwave vessel, 3 mL of His (0.1 M) was added over 1.5 mL of HAuCl4 (10 mM) and the mixture was introduced in the microwave reactor. Afterwards, it was irradiated with microwaves at 850 W for 30 min at 90°C and 1200 rpm.

4.3.2. Characterization of His-AuNCs

The colloidal solution of the His-AuNCs obtained *via* a microwave assisted approach is presented in the inset of **Figure 4.6**. The color of the solution was pale-green under ambiental light excitation, which turned blue under UV excitation, proving that His-AuNCs are empowered with intrinsic photoluminescence. The colloidal solution of His-AuNCs exhibit an excitation peak located at 380 nm and a corresponding bright-blue photoluminescence localized at 471 nm. Furthermore, compared to the photoluminescence of His-AuNCs prepared using a procedure from literature [33], the proposed microwave-assisted synthesis resulted in the preparation His-AuNCs that present am enhanced photoluminescence by four times under the same 380 nm excitation. The photoluminescence of His-AuNCs has maintained over 91% of its initial intensity under continuous irradiation at 380 nm for 15 min, demonstrating its high photostability.

4.3.3. Performance of His-AuNCs-based colloidal sensor

After the selectivity assays, in the presence of different common metal ions, a quenching effect of the His-AuNCs photoluminescence was observed after their interaction with Fe ions. The mechanism explaining the photoluminescence quenching effect might be related to Fe-induced aggregation of the NCs. The aggregation can take place due to a coordination together with a cross-linking of the carboxyl and amino groups powered by Fe ions [47,48]. Further, the sensitivity of the colloidal sensor towards the Fe ions detection was investigated by incubating them with increasing concentrations of Fe ions from 0 to 44 mM. The linear fit exposed the linear dynamic range of the His-AuNCs-based sensor ranging from 0.022 to 4.4 mM and the limit of detection was calculated to be 0.2 μM. Taking in consideration that the maximum accepted concentration of Fe ions in water according to World Health Organization is 35 μM [49], the His-AuNCs colloidal-sensor is suitable to prevent dangerous intakes of Fe ions from drinking water.

4.3.4. Fe ions sensing using His-AuNCs-paper-based platform

4.3.4.1. In laboratory conditions

As it was demonstrated, the performance of His-AuNCs as a sensing platform for the detection of Fe ions is outstanding. However, this approach presents some drawbacks such as low accessibility, low portability, time-consuming and is mandatory to be performed by trained

personnel. Therefore, the His-AuNCs were integrated on Whatman filter paper in order to develop a cheap, fast and portable sensing platform for the selective identification and quantification of Fe ions from water, as briefly presented in **Scheme 4.1.**

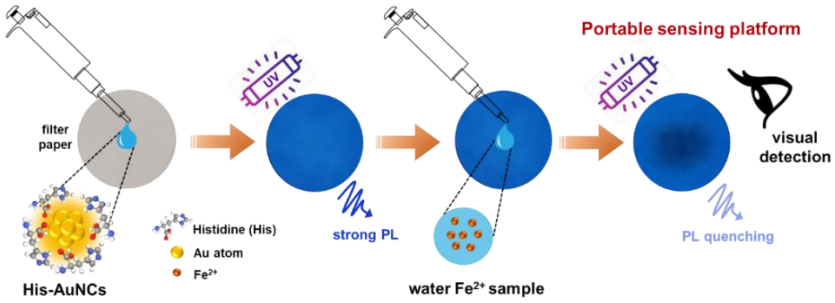

Scheme 4.1. *Schematic representation of the His-AuNCs@paper-based sensor's fabrication together with the viasual detection of Fe ions. Scheme reproduce from* [44].

Specifically, the colloidal solution of His-AuNCs was drop-casted on Whatman filter paper and was left to dry for 24 h in order to fabricate the His-AuNCs@paper-based sensing platform. Next, 5 µL drops of Fe ions solutions with concentrations ranging from 0 to 123 µM were dropped over the active detection spots of the His-AuNCs@paper-based sensor. The photoluminescence quenching of impregnated-His-AuNCs was visually evaluated after 15 minutes under UV light and photos were acquired using the camera of a smartphone (**Figure 4.3**)

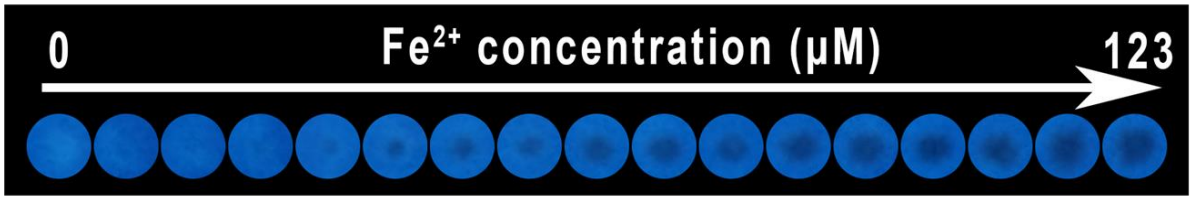

Figure 4.3. *Photos of the His-AuNCs@paper-based sensing platform recorded under UV light, 15 min after the sensors' incubation with Fe ions at concentrations ranging from 0 to 123 µM. The detection spots were previously dried for 1 day. Figure adapted from* [44].

The control detection spot, treated only with ultrapure water, exhibited no changes in intensity or color (first detection spot in **Figure 4.3**). However, the detection spots that were contaminated with rising concentration of Fe ions present a visually detectable change in color in the middle induced by the interaction between the Fe ions and the impregnated-His-AuNCs.

Explicitly, the color in the middle of the detection spot changes from bright blue to gray-blackish, as the sensing platform interacts with higher concentrations of Fe ions, demonstrating that the His-AuNCs@paper-based sensor is capable to detect Fe ions. Moreover, the dark spot increases in diameter as the concentrations of Fe ions increases, proving that the sensor is also sensitive, not only qualitative, towards the detection of Fe ions from water. Therefore, the blue intensity of the Fe-contaminated detection spots was extracted using ImageJ software and were plotted compared to the blue intensity of the control (I/I_0) against the concentration of Fe ions from 0 to 123 μM. After fitting operations, the average blue intensity plot against the concentration of Fe ions exposed a linear dynamic range from 9 to 97 μM and a limit of detection of 3.2 μM, demonstrating that the His-AuNCs-impregnated paper-based sensor is relevant for the detection of harmful levels of Fe ions.

4.3.4.2. From real water samples

Once the ability of the His-AuNCs-impregnated paper-based sensing platform to selectively and sensitively detect Fe ions in laboratory conditions was demonstrated, the next step was to evaluate its capacity to detect and quantify Fe ions from real water samples. For these experiments, the water samples were collected from local sources like spring, river and tap water and 5 μL were dropped over the active detection spot of the paper-based sensor. For the local tested river, spring and tap waters, no traces of Fe ions were depicted by the His-AuNCs@paper-based sensor, therefore, the samples were spiked with 35 μM of Fe ions and the assays were further performed. After a visual investigation, a dark photoluminescence quenching of the impregnated-His-AuNCs was observed, similar to the one obtained with the same concentration but in laboratory conditions. Furthermore, the average blue intensity were extracted using the ImageJ software and the concentration of Fe ions detected by the His-AuNCs@paper-based sensing platform was calculated and recoveries ranged between 102.0 and 105.4% were obtained, which demonstrates the excellent accuracy of the sensor even when tested on real water samples.

4.3.5. Conclusions

To conclude, a novel, fast and cheap His-AuNCs-impregnated paper-based sensing platform was developed for the selective detection and quantification of dangerous concentrations of Fe ions from real water samples. The His-AuNCs were synthesized *via* a novel microwave-assisted approach with a blue intrinsic photoluminescence located at 471 nm under excitation at

380 nm. Further, the selectivity of the His-AuNCs colloidal solution towards the detection of Fe ions was proved, while the sensitivity assays exposed a linear dynamic range from 0.022 to 4.4 mM together with a limit of detection as low as 0.2 μM. Next, the His-AuNCs were impregnated on Whatman filter paper in order to fabricate an accessible, easy-to-use and portable sensing device for the accurate detection and quantification of Fe ion from low-volume water samples. To achieve a quantification of the Fe ions, photos of the active detection spots were acquired using a smartphone camera and the average blue intensity was extracted and plotted against the concentration of Fe ions. After fitting operations, a linear dynamic range from 9 to 97 μM was obtained and a limit of detection of 3.2 μM was calculated. Moreover, the selectivity and competitivity assays proved the high specificity and accuracy of the paper-based sensor. Finally, the His-AuNCs-impregnated paper-based sensor was validated using spiked real water samples, returning recoveries ranging from 102.0% to 105.4%. In view of future applications, photos of the His-AuNCs@paper-based sensor after interaction with the water sample can be acquired using a smartphone camera and afterwards sent to an accredited environmental monitoring institution to perform the analysis. Therefore, the His-AuNCs@paper-based sensor represents a promising candidate as an accurate lab-on-a-chip device for the fast and cheap detection of harmful concentrations of Fe ions from real water environments.

Part II. Contributions on the synthesis of new noble metal nanoparticles for applications as SERS contrast agents, nanoantibiotics and sensing platforms

Chapter 5. Polymeric cyclodextrin bimetallic core-shell nanoparticles as nanoantibiotics and SERS contrast agents

5.1. Introduction

Bimetallic nanoparticles (BMNPs) represent a new class of nanoobjects that merge the properties of two different metals in one empowered NP. In the past decade, they generated huge interest due to their ability to be used in multiple applications such as nanomedicine, biosensing, surface enhanced Raman scattering (SERS), imaging and catalysis [14,50–54]. However, their physico-chemical properties together with their biological properties weren't fully explored yet [55]. By combining two metals, an alteration in their electron density is induced, therefore, due to their unique optical electronic, thermal and catalytic features, BMNPs were reported to be superior to monometallic NPs [56,57]. Moreover, metal ratio, time and temperature are the parameters that can influence the internal distribution of the BMNPs and structures such as homogeneous alloys, core-shell or something in-between can be obtained. However, the timing of the reduction is the key parameter in controlling the internal structure of BMNPs as if both metal ions are reduced simultaneously an alloy will be obtained, while if they are reduced in two different steps, a core-shell structure will be obtained [58].

5.2. Syntesis of PolyCD-Au@AgNPs

PolyCD-Au@AgNPs were synthesized using a two-step procedure: (1) the gold-core synthesis – by mixing 1.5 mL of $HAuCl_4$ (10^{-3} M) with 9 mL of PolyCD (aqueous solution - 2 mg/mL) under magnetic stirring at 70 °C, obtaining PolyCD stabilized gold NPs (PolyCD-AuNPs); and (2) the silver-shell deposition – to 5 mL of PolyCD-AuNPs were added 30 µL of ascorbic acid (0.1 M) and 10 µL of $AgNO_3$ (0.1 M) under magnetic stirring for 1h and the addition was repeated for two more times, resulting in an orange colloidal solution containing PolyCD-Au@AgNPs. The as-prepared NPs were purified by centrifugation at 6000 rpm for 10 min and were redispersed in water. The colloidal solution was kept at 4°C until further use

5.3. Characterization of PolyCD-Au-AgNPs

The core-shell Au-Ag NPs stabilized by PolyCD were synthesized *via* a two-step procedure. First, AuNPs were prepared according to the procedure presented in subsection 5.2.2

after which the color of the colloidal solution turned purple (inset – **Figure 5.1**) and a LSPR band localized at 527 nm was depicted in the UV-Vis spectrum (black line – **Figure 5.1**), which is typical to AuNPs.

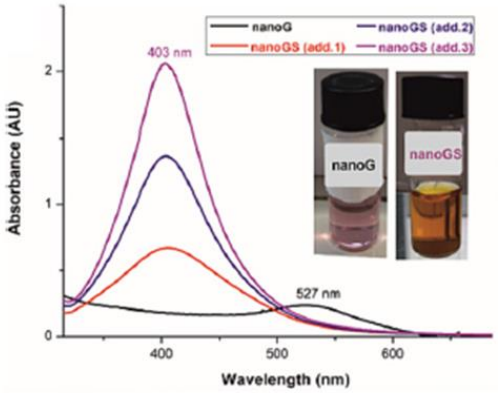

Figure 5.1. *The UV-Vis spectra of PolyCD-AuNPs (nanoG) and PolyCD-Au-AgNPs (nanoGS) after each addition of $AgNO_3$ aliquots (inset - photo of the colloidal solutions of PolyCD-AuNPs and PolyCD-Au-AgNPs). Figure adapted from* [59].

Next, three successive additions of $AgNO_3$ aliquots were performed and the color of the colloidal solution turned orange-brownish, while the UV-Vis spectrum broadened and increased its intensity. Moreover, the LSPR band shifted to 403 nm, which was previously observed for core-shell Au@AgNPs and is due to the new type of plasmon resonance which occurs for the electrons oscillating at the interface of the of the Au-core and the Ag-shell [14]. Furthermore, the morphology of the novel Au and Au@Ag nanostructures was evaluated using the TEM technique. The PolyCD-AuNPs present a spherical shape with an average size of 8 ± 3 nm, calculated after measuring more than 300 NPs. Moreover, after the final addition of $AgNO_3$, the formation of an Ag-shell was observed from the recorded TEM images. Specifically, the dark Au-core can be easily distinguished from the brighter Ag-shell which was uniformly formed around the core. The difference in black-shade of the Au-core and the Ag-shell is due to the electron density differences between the two elements. The average size of the PolyCD-Au@AgNPs was calculated to be 11 ± 3 nm, proving that the average thickness of the Ag-shell is around 1.5 nm.

5.4. Linezolid-conjugated PolyCD-Au@AgNPs as an efficient nanoantibiotic

Zone inhibition assay was performed to investigate the antibacterial activity of PolyCD-Au@AgNPs against different bacterial strains such as *S. aureus, E. coli, P. aeruginosa* different inhibition areas were found against all the tested bacteria strains, while no antibacterial activity was found for PolyCD and PolyCD-AuNPs alone. Taking in consideration that core-shell NPs were found to possess good antibacterial activity against *E. coli*, the PolyCD-Au@AgNPs were conjugated with Lz, an antibiotic that is approved for the treatment against Gram-positive bacterial infections [60]. The new Lz-conjugated PolyCD-Au@AgNPs (nanoGS-Lz) were prepared by the hydration of a Lz organic film with colloidal solution of PolyCD-Au@AgNPs at a molar ratio between cyclodextrin and Lz of 1:1, 1:0,5 and 1:0,25. Next, the antibacterial activity profile of nanoGS-Lz was evaluated against Gram-negative strains such as E. coli and *P. aeruginosa* together with Gram-positive strains like *S. aureus* together with its methicillin resistant form (MRSA). Lz and PolyCD-Au@AgNPs were used as controls in these experiments. The MIC and MBC were investigated *via* the broth microdilution approach. The Lz antibiotic exhibited bacteriostatic activity, as expected, against the Gram-positive strains (*S. aureus* and the MRSA strain of *S. aureus*) with a MIC calculated at 0.97 µg/mL and 1.95 µg/mL, respectively. The new nanoGS-Lz complexes presented a broader antibacterial activity compare to PolyCD-Au@AgNPs alone, while the Lz1 and Lz2 complexes turned out to be most efficient. The last-mentioned ones exhibited an excellent antibacterial activity against all the tested Gram-positive and Gram-negative strains. In particular, all nanoGS-Lz complexes were bactericidal against the Gram-negative strains (*E. coli* and *P. aeruginosa*), while against the Gram-positive strains (*S. Aureus* together with the MRSA form) bactericidal activity was observed only for the complexes with a higher Lz/Ag molar ratio (nanoGS-Lz1 and nanoGS-Lz2). Their efficiency against the *S. aureus* and the MRSA strains strictly depends on the Lz concentration, as the MIC didn't decrease with the increase of Ag concentration. Moreover, the complexation of Lz with PolyCD-Au@AgNPs resulted in a MIC increase against *S.aureus* and the MRSA strains compared to Lz alone due to the most probably slower release of the Lz which is included in the cyclodextrin cavity. Overall, the antibacterial assays proved the crucial role of positively charged cyclodextrin in the antibacterial activity of PolyCD-Au@AgNPs. Specifically, PolyCD improves the adsorption of the NPs on the bacterial wall by electrostatic attraction with the negatively-charged teichoic acids of Gram-positive bacteria and the lipopolysaccharides of Gram-negative bacteria. Additionally, the silver ions

released by the PolyCD-Au@AgNPs produced a malfunction of the Gram-negative bacteria's wall killing it eventually, while the complexation of Lz with PolyCD-Au@AgNPs was crucial for killing the Gram-positive bacteria.

5.5. PolyCD-Au-AgNPs as SERS contrast agents

In order to get better understanding on where do the proposed NPs accumulate inside cells, the PolyCD-Au@AgNPs were functionalized with a Raman reporter molecule (SERS-nanoTag) in order to be tracked *via* a confocal Raman microscope. After proving their biocompatibility, the next step was to investigate the cellular uptake, distribution and localization of the newly-prepared SERS-nanoTags inside living ovarian adenocarcinoma cells (NIH:OVCAR-3) using confocal scanning Raman microscopy under excitation at 532 nm and the acquired Raman images together with the corresponding bright-field image of the cell are presented in **Figure 5.2**.

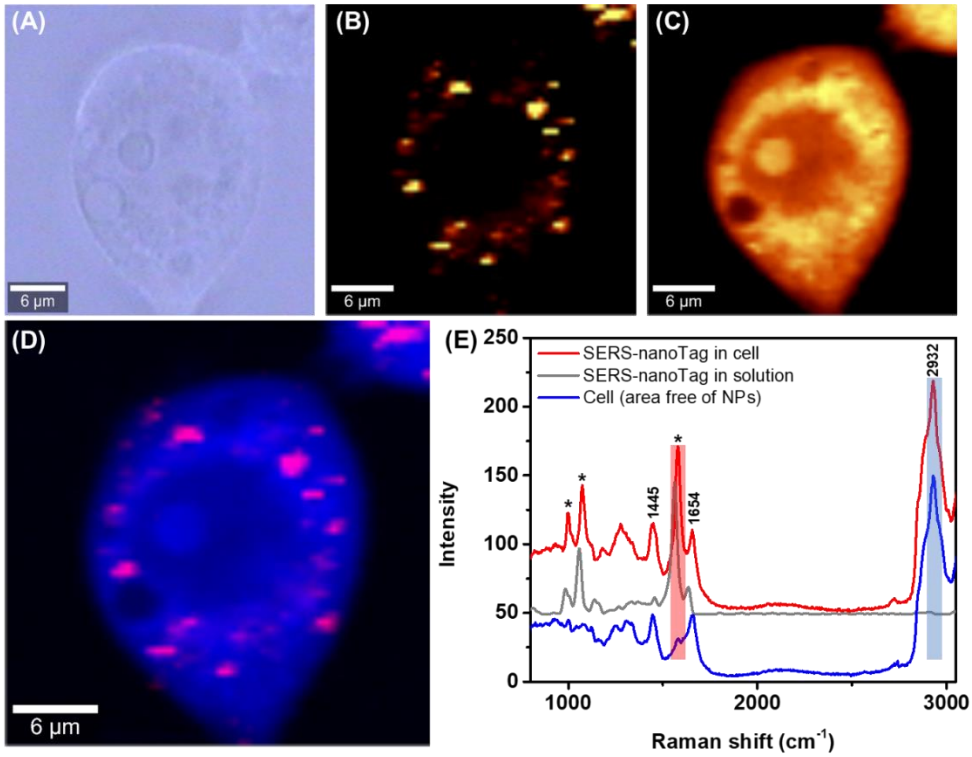

Figure 5.2. *(A) The bright field image of the ovarian adenocarcinoma NIH:OVCAR-3 cell incubated with the prepared SERS-nanoTag. The Raman maps of the same cell which was generated by plotting the intensity of the (B) 1574 cm^{-1} and (C) 2800-3100 cm^{-1} peaks acquired under 532 nm excitation. (D) An overlay image of the Raman maps from image (B) and (C). (E) The Raman spectra extracted from an area of the cell containing SERS-nanoTags (red line) and free of SERS-nanoTags (blue line) compared to the*

SERS spectrum of the SERS-nanoTags in colloidal solution under 532 nm excitation. Figure reproduced from [59].

The structure of the cell was imaged by plotting the intensity of the 2800-3100 cm^{-1} peak attributed to the lipids C-H stretching vibrations (**Figure 5.2.C**), while the SERS-nanoTag's distribution and localization in the same NIH:OVCAR-3 cell was obtained by plotting the intensity of the 1574 cm^{-1} peak, the brightest peak of the SERS-nanoTags fingerprint signal (**Figure 5.2.B**). By overlaying the two generated Raman maps (**Figure 5.2.D**), a high intracellular internalization of the SERS-nanoTags (red area) was observed inside the scanned NIH:OVCAR-3 cell (blue area). The PolyCD-Au@AgNPs are well distributed inside the cell's cytoplasm, mostly around the nucleus, but not penetrating its membrane. Next, a Raman spectrum was extracted from the are free of SERS-nanoTags which presents the typical signal of the intracellular components. In particular, the 1445 cm^{-1} band was assigned to C-H deformation vibrations, while the ones at 1654 and 2932 cm^{-1} were attributed to C=C stretching vibrations from the lipids and the symmetric CH_3 stretching vibrations from the proteins, respectively. Furthermore, the SERS spectrum extracted from the area of the cell with SERS-nanoTAgs (red area) depicts both the cell's typical Raman signal and the SERS fingerprint of MPBA. Specifically, the most intense peaks at 1000, 1068 and 1574 cm^{-1} represent specific bands of the MPBA which were depicted in the measurements performed in colloidal solution, while the peaks at 1445, 1654 and 2932 cm^{-1} are specific vibrational model of the lipids and proteins inside the cell. Overall, the aforementioned results prove that MPBA-functionalized PolyCD-Au@AgNps are promising candidates as bright and reliable SERS contrast agents for intracellular imaging applications.

5.6. Conclusions

In this chapter, PolyCD-stabilized core@silver Au@Ag NPs were synthesized using a two-step approach by exploiting the unique features of the cationic cyclodextrin polymer. Specifically, the UV-Vis spectroscopy measurements performed on PolyCD-AuNPs depicted one LSPR band located at 527 nm, while after the addition of $AgNO_3$, a LSPR band localized at 408 nm was depicted, indicating the formation of PolyCD-Au@AgNPs. The spherical core-shell structure of the prepared NPs was confirmed using TEM, while the size histogram revealed an 8 nm Au-core and a 1.5 nm Ag-shell. Moreover, the PolyCD-Au@AgNPs present high stability in time and under

UV irradiation, which is mostly due to the multiple functionalities of the stabilizing cyclodextrin polymer such as epichlorohydrin chains and the functional charged-groups on each cyclodextrin unit. Furthermore, nanoantibiotics were prepared by the complexation of Lz with PolyCD-Au@AgNPs exhibiting excellent antibacterial activity against all the tested Gram-positive and Gram-negative strains including the MRSA. The new Lz-based nanoantibiotic shower improved activity compare to PolyCD-Au@AgNPs and Lz alone. In addition, the PolyCD-Au@AgNPs present excellent biocompatibility against ovarian adenocarcinoma NIH:OVCAR-3 cells, therefore, they were functionalized with a Raman reporter molecule, MPBA. The ability of the newly prepared SERS-nanoTags to perform as bright contrast agents with accurate localization inside a single-cell level was proved by the cell imaging assays under confocal scanning Raman microscopy.

Chapter 6. Aptamer-functionalized gold nanoparticles for the colorimetric detection of C-reactive protein

6.1. Introduction

As morbidity and mortality caused by a local organ infection have, unfortunately, increased in the past decades, therefore, the early diagnosis is crucial in order to prevent inflammation or to manage diseases caused by inflammatory infections. Lately, the prognosis, diagnosis and even the treatment of inflammatory infections or inflammation are corelated to biomarkers from biological samples that are measurable. Human C-reactive protein (CRP) is considered an early clinical marker which indicates the presence of inflammatory or infectious conditions corelated to different kinds of diseases or pathological conditions like viral and bacterial infections, sepsis, cardiovascular diseases, etc [61]. Therefore, humans with blood serum containing CRP levels lower than 10 μg/mL are inflammation free, if the human has a viral infection the CRP levels increase between 10 to 40 μg/mL, for a bacterial infection the levels are between 40 and 200 μg/mL, while in the unfortunate case of sepsis CRP spikes above 200 μg/mL [62]. Moreover, humans which exhibit chronically low levels of CRP (below 5 μg/mL) present high risks to develop coronary hearth diseases, acute myocardial infarction and even ischemic stroke, therefore, CRP analysis plays a crucial role in preventing these diseases [63]. However, the current methods for the accurate detection of CRP like ELISA, chemiluminescent assay or immunoturbidimetric assay are complex, time-consuming, extremely expensive, needs highly-trained personnel making them not suitable for point-of-care clinical diagnosis. Therefore, there is a high necessity to develop newer, faster and cheaper methods to detect CRP from human serum.

6.2. Synthesis of Cit-AuNPs

The gold nanoparticles were synthesized using the Turkevich-Frens approach based on the reduction of Au^{3+} by the sodium citrate. Briefly, 100 mL of $HAuCl_4$ (10^{-3} M) was brought to boiling under magnetic stirring, moment at which 12 mL of sodium citrate (38.8×10^{-3} M) was added and left 15 minutes to stir with the heat on and 15 minutes with the heat off.

6.3. Characterization of Cit-AuNPs

Citrate-stabilized AuNPs (Cit-AuNPs) were synthesized using the Turkevich-Frens procedure. The Cit-AuNPs exhibit a narrow LSPR band located at 520 nm, a typical optical response of spherical AuNPs. Afterwards, the morphological properties of the Cit-AuNPs were investigated using TEM and the Cit-AuNPs present a spherical shape with an average size of 15 ± 1 nm, demonstrating that the Cit-AuNPs are highly monodisperse.

6.4. Functionalization of Cit-AuNPs with CRP specific aptamer

The aptamer with a high affinity towards CRP is in fact an oligonucleotide with the following sequence 5′-CGA AGG GGA TTC GAG GGG TGA TTG CGT GCT CCA TTT GGT G-3′. In the absence of the target protein, the aptamer, a single stranded DNA sequence, interacts with the citrate from the surface of the AuNPs. Therefore, in order to obtain a sensing platform with high affinity towards the CRP, the Cit-AuNPs were incubated with aptamer at 20 °C in an orbital vortex. After 10 min of incubation with aptamer, no change in the Cit-AuNPs' LSPR response was observed, proving that their stability was preserved after the interaction with the aptamer. Moreover, the absorbance band specific to the aptamer localized at 260 nm appeared after the incubation. Finally, to validate the functionalization of Cit-AuNPs with the aptamer specific to CRP, a stability test in the presence of PBS and NaCl of the colloidal solution was performed. In the case of the Cit-AuNPs that were not incubated with the aptamer, a significant aggregation was observed in the UV-Vis spectrum by the rising absorption of the colloidal solution in the 600-900 nm wavelength range. However, the apta-Cit-AuNPs exhibit no significant changes in their LSPR response in the presence of PBS and NaCl, proving their high stability and, therefore, the successful functionalization of Cit-AuNPs with an aptamer with high affinity towards CRP protein.

6.5. Performance of aptamer-functionalized Cit-AuNPs towards CRP detection

The aptamer, a single stranded DNA, exhibits high affinity to the CRP protein. Thus, when CRP is added in the colloidal solution of Cit-AuNPs in the presence of a saline solution, the

aptamer desorbs from the surface of the NPs and interacts preferentially with the CRP protein, leaving the NPs exposed to salt (**Scheme 6.1**).

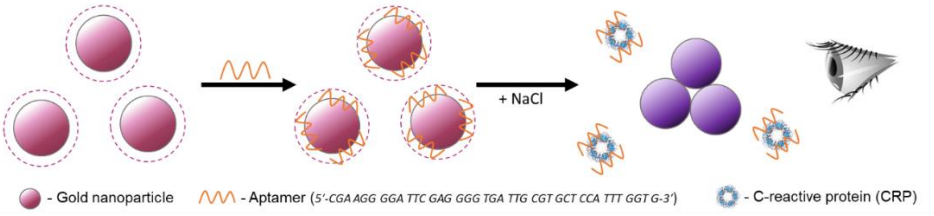

Scheme 6.1. *Schematic representation of the colorimetric detection mechanism of CRP using the apta-Cit-AuNPs.*

A salty environment disrupts the repulsion effects between the aptamer-free Cit-AuNPs and promotes their aggregation which is accompanied by a change in color of the colloidal solution. Following the aforementioned strategy, upon the colloidal solution of apta-Cit-AuNPs, different concentration of CRP ranging between 1 and 100 µg/mL were added in the presence of a high concentration of NaCl and were left to incubate for 10 min. First, as the incubated concentration of CRP increased, a gradual change in color of the colloidal solution was observed from burgundy red to light purple (**Figure 6.1.A**), proving the ability of the apta-Cit-AuNPs to perform as a colorimetric sensor towards the detection of CRP.

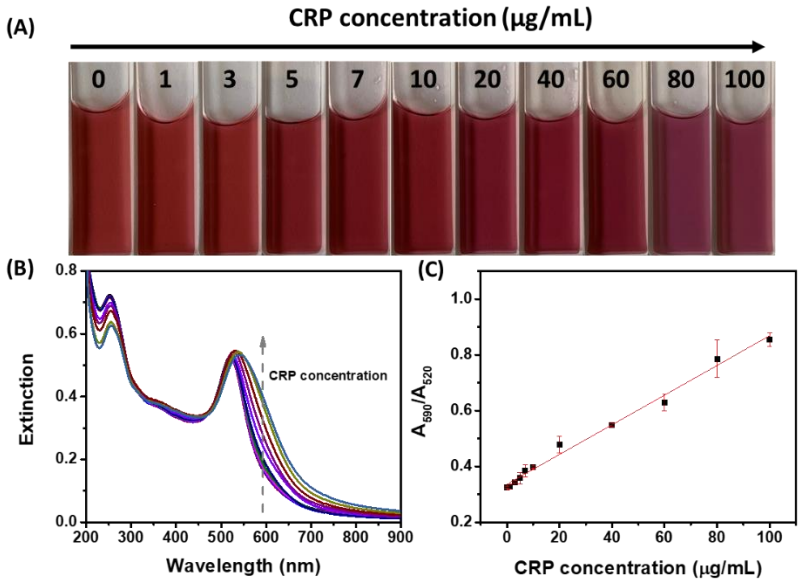

Figure 6.1. *(A) Photographic images and (B) the corresponding extinction spectra of the colloidal solutions of apta-Cit-AuNPs incubated with different concentration of CRP (0-100 µg/mL) in the presence*

of NaCl. (C) The absorption ratio between the LSPR band at 590 nm (aggregated NPs) and 520 nm (individual NPs) as a function of CRP concentration together with the corresponding linear fit which reveal the linear dynamic range between 1 and 100 μg/mL.

The control sample represents the apta-Cit-AuNPs incubated with the equivalent volume of PBS only, instead of the CRP-PBS solution and exposed to the same amount of NaCl solution. The colloidal solutions of CRP-incubated apta-Cit-AuNPs were analyzed using UV-Vis spectroscopy. The addition of increasing concentration of CRP in the colloidal solution of apta-Cit-AuNPs in the presence of NaCl resulted into a gradual broadening of the LSPR band together with an increased-extinction in the 650-800 nm wavelength region, confirming the aggregation strategy proposed above. Next, the absorption ratio between the LSPR band located at 590 nm (attributed to aggregated NPs) and the one localized at 520 nm (specific to individual NPs) was plotted against the corresponding CRP concentration and the results are presented in **Figure 6.3.C**. The performed fitting operations revealed a linear dynamic range between 1 and 100 μg/mL and a limit of detection of 2.64 μg/mL. It is worth mentioning that the detection time is only 10 min, while a normal laboratory CRP analysis could take even days, while the price is significantly higher. Moreover, the apta-Cit-AuNPs-based procedure is capable to detect both low and high concentrations of CRP integrating both the standard CRP analysis and the high sensitivity CRP analysis in a single sensing procedure.

Taking in consideration that the human serum contains various substances such as protein, electrolytes, antibodies, antigens, hormones but also exogenous substances such as microorganisms and drugs which could possibly interact or even deteriorate the accuracy of the proposed sensor, a selectivity assay was performed. Thus, the colloidal solution of apta-Cit-AuNPs was incubated with various substances that can be found in the human serum like HSA, AA, urea, myoglobin, L-glutamine, CRP but also substances that simulate the human serum such as PBS and SBF-HSA. The colloidal solutions of apta-Cit-AuNPs incubated with PBS (CTR), HSA, SBF, AA, urea, L-glutamine (glu) and myoglobin (myog) in the presence of NaCl exhibit no significant changes in their color compared to the ones incubated with CRP which turns from red burgundy to dark red, demonstrating the high selectivity of the proposed sensor towards the detection of CRP.

6.6. Conclusions

In this chapter, a simple, fast and cheap colorimetric procedure for the selective detection and quantification of CRP was developed based on salt-induced aggregation effects of aptamer-functionalized Cit-AuNPs. The Cit-AuNPs synthesized using the Turkevitch-Frenc method with narrow LSPR band at 520 nm were functionalized with a CRP specific aptamer for the fast (10 min) and selective detection of CRP on a broad range of concentrations using relatively cheap equipment (UV-Vis spectrometer). The quantification of CRP was obtained by plotting and fitting the intensity ration between the LSPR bands of aggregated (590 nm) and individual NPs (520 nm) against the corresponding CRP concentrations, revealing a linear dynamic range between 1 and 100 μg/mL and a limit of detection as low as 2.64 μg/mL. Beside the faster times and cheaper analysis, this approach managed to detect both low and high concentration of CRP, integrating both the standard CRP analysis and the high sensitivity CRP analysis in a single sensing procedure. Therefore, the Cit-AuNPs functionalized with a CRP specific aptamer represent a promising sensing platform that is suitable for fast point-of-care clinical diagnosis.

Chapter 7. Final Conclusions and Perspective

The aim of this work was to investigate the feasibility of noble metal NCs and NPs to be successfully integrated in the development of contrast agents and sensing platforms and their potential implementation in various medical and environmental applications. To achieve the proposed objectives, each nanomaterial presented in this thesis was in detail investigated from their novel or adapted synthesis, to their in-depth characterization and in the end their proof-of-concept implementation as contrast agents in fluorescence or SERS *in vitro* and even simulated *ex vivo* imaging (tissue mimicking phantoms) and as sensing platforms for the detection of heavy metal ions (Cu and Fe ions) or C-reactive protein was demonstrated.

Final Conclusions

The final conclusions of this work are the following:

1) AuNCs embedded inside a bovine serum albumin corona with an average size of 3 nm and an intense red intrinsic photoluminescence were synthesized using an adapted procedure. The thorough fluorescence investigations *via* the steady-state and time-resolved fluorescence techniques revealed their two emission processes: prompt fluorescence and temperature-activated delayed fluorescence. Afterwards, their functionalization with folic acid, increased their biocompatibility as viability assays proved, while empowering them with the ability to target FRα-overexpressed cells as demonstrated by both conventional and fluorescence lifetime imaging microscopy under one-photon excitation. Finally, the ability of BSA-AuNCs to perform as fluorescent contrast agents inside tissue-mimicking agarose-phantoms, a bioethical step before *in vivo* experiments, was demonstrated *via* near-infrared two-photon excitation FLIM.

2) Glutathione-stabilized AuNCs were successfully synthesized using a novel microwave-assisted procedure. The steady-state spectroscopy revealed a dual emission: a red photoluminescence at 610 nm and a NIR one at 800 nm under 405 nm excitation. The photoluminescence of GSH-AuNCs was thoroughly investigated using the FLIM technique, which revealed beside the long lifetime of each of the emission, even an energy transfer between the two emissions. Moreover, GSH-AuNCs were proven to be photostable and intensively emissive under a wide range of wavelengths including 640 nm, which is in the first biological window, making

them suitable for imaging applications. Finally, the FLIM assays performed on GSH-AuNCs embedded in tissue mimicking agarose-phantoms proved that GSH-AuNCs are promising candidates as NIR-emitting contrast agents in future *ex vivo* and *in vivo* imaging applications.

3) AuNCs impregnated in Whatman filter paper were proven to be excellent in the cheap, fast and selective detection of heavy metal ions such as Cu and Fe ions from real water samples. First, the photoluminescence of colloidal BSA-AuNCs was proven to quench selectively in the presence of Cu ions. Afterwards, the colloidal sensor was transferred on filter Whatman paper and was exposed to different concentrations of Cu ions, revealing the capacity of the novel BSA-AuNCs@paper-based platform to perform as a semi-quantitative sensor for the detection of Cu ions by the naked-eye. Secondly, histidine-stabilized AuNCs were impregnated on filter paper and, after 1 day of drying, the detection spots were exposed to common heavy metal ions, revealing the selective quenching in the presence of Fe ions. Moreover, by analyzing using the ImageJ software the photographic images of the His-AuNCs@paper sensor exposed to different concentration of Fe ions, an accurate quantification in the 9-97 μM range was achieved. Furthermore, the accuracy of both sensing platforms was confirmed using real water samples. Therefore, the NCs-paper platforms represent efficient lab-on-a-chip devices for on-site monitoring of dangerous levels of heavy-metal ions in real water samples.

4) Polymeric cyclodextrin core-shell Au@AgNPs were proven to be efficient nanoantibiotics and reliable SERS contrast agents. The NPs were successfully synthesized *via* a two-step procedure obtaining a 8 nm Au-core surrounded by a 1.5 nm Ag-shell, as proven by TEM. Their stabilization with PolyCD empowered them with the capacity to incapsulate, in their cyclodextrin cavity, drugs or antibiotics such as Linezolid. The complexation of Lz to PolyCD-Au@AgNPs resulted in the broadening of their antimicrobial activity against both Gram-positive and Gram-negative strains including the methicillin-resistant *Staphylococcus aureus*. Moreover, by functionalization with 4-mercaptophenylboronic acid, the biocompatible PolyCD-Au@AgNPs were easily tracked inside live ovarian adenocarcinoma cells *via* confocal Raman microscopy and therefore, proved the capacity to perform as bright and reliable SERS contrast agents.

5) The colorimetric detection of C-reactive protein, a cardiovascular and inflammation marker, was achieved using citrate-stabilized AuNPs functionalized with a CRP specific aptamer. First, the Cit-AuNPs were functionalized with a single strained DNA-based aptamer, which

empowered them with high stability against high concentration of NaCl. However, after the addition of CRP, the aptamer preferentially interacted with CRP, detaching from the NPs. The salt-exposed aptamer-free NPs aggregated which resulted a change in color of their colloidal solution. Exposing the apta-Cit-AuNPs to higher concentration of CRP, resulted into a higher-level of agglomeration. Therefore, by analyzing the colloidal solution's aggregation-level *via* UV-Vis spectroscopy, it revealed a wide linear detection range between 1 and 100 µg/mL. Therefore, the apta-Cit-AuNPs were proved to be a fast, cheap and efficient sensing platform for the selective detection and quantification of C reactive protein

Perspectives

Taking in consideration the work performed in this thesis, in the near future I would like to:

- investigate the potential of both BSA-AuNCs and GSH-AuNCs as photoluminescent contrast agents for *in vivo* imaging applications (e.g. image-assisted surgery);
- develop a fast, cheap and accurate NCs@paper-based sensor for the selective detection and quantification of pesticides from fruits and vegetables;
- investigate the NCs potential as antimicrobial agents;
- study the interaction between NCs and NPs towards metal-enhanced fluorescence emission;
- test the CRP-detection accuracy of the apta-Cit-AuNPs' sensor from real human samples;

Dissemination of the results

List of publications related to the doctoral thesis

List of ISI publications

1) Folic acid functionalized gold nanoclusters for enabling targeted fluorescence imaging of human ovarian cancer cells, **A.-M. Hada**, A.-M. Craciun, M. Focsan, R. Borlan, O. Soritau, S. Astilean, **Talanta** 225 (2021) 121960-121968 (IF 6.556, AIS 0.765), 35 Citation (Google Scholar);

2) Intrinsic photoluminescence of solid-state gold nanoclusters: towards fluorescence lifetime imaging of tissue-like phantoms under two-photon near-infrared excitation, **A.-M. Hada**, A.-M. Craciun, A. Simion, **Frontiers in Chemistry** 9 (2021) 761711 (IF 5.545, AIS 0.937), 4 Citations (Google Scholar);

3) Gold nanoclusters performing as contrast agents for non-invasive imaging of tissue-like phantoms via two-photon excited fluorescence lifetime imaging, **A.-M. Hada**, A.-M. Craciun, A. Simion, **Analyst** 146 (2021) 7126-7130 (IF 5.227, AIS 0.778), 3 Citations (Google Scholar);

4) Glutathione-capped gold nanoclusters as near-infrared-emitting efficient contrast agents for confocal fluorescence imaging of tissue-mimicking phantoms, **A.-M. Hada**, A.-M. Craciun, M. Focsan, A. Vulpoi, E.-L. Borcan, S. Astilean, **Microchimica Acta** 189 (2022) 337 (IF 5.7, AIS 0.739), 2 Citations (Google Scholar);

5) Novel paper-based sensing platform using photoluminescent gold nanoclusters for easy, sensitive and selective naked-eye detection of Cu^{2+}, **A.-M. Hada**, M. Zetes, M. Focsan, T. Nagy-Simon, A. M. Craciun, **Journal of Molecular Structure**, 1244 (2021) 130990 (IF 3.841, AIS 0.315), 11 Citations (Google Scholar);

6) Photoluminescent Histidine-Stabilized Gold Nanoclusters as Efficient Sensors for Fast and Easy Visual Detection of Fe Ions in Water Using Paper-Based Portable Platform, **A.-M.**

Hada, M. Zetes, M. Focsan, S. Astilean, A.-M. Craciun, **International Journal Molecular Sciences** 23 (2022) 12410 (IF 5.6, AIS 1.028), 1 Citation (Google Scholar);

7) Recent advances on the development of plasmon-assisted biosensors for detection of C-reactive protein, T. Nagy-Simon, **A.-M. Hada**, S. Suarasan, M. Potara, **Journal of Molecular Structure** 1246 (2021) 131178 (IF 3.841, AIS 0.315), 7 Citations (Google Scholar);

8) Linezolid nanoAntiobiotics and SERS-nanoTags based on polymeric cyclodextrin bimetallic core-shell nanoarchitectures, **A.-M. Hada**, M. Potara, S. Astilean, A. Cordaro, G. Neri, M. Malanga, A. Nostro, A. Mazzaglia, A. Scala, A. Piperno, **Carbohydrate Polymers** 293 (2022) 119736 (IF 11.2, AIS 1.238), 8 Citations (Google Scholar);

Manuscripts in preparation

1) Aptamer-functionalized gold nanoparticles for the highly-sensitive dual-detection of C-reactive protein, **A.-M. Hada**, S. Suarasan, M. Potara, S. Astilean;

Other publications

1) Fabrication of gold-silver core-shell nanoparticles for performing as ultrabright SERS-nanotags inside human ovarian cancer cells, **A.-M. Hada**, M. Potara, S. Suarasan, A. Vulpoi, T. Nagy-Simon, E. Licarete, S. Astilean, **Nanotechnology** 30 (2019) 315701-315711 (IF 3.5, AIS), 25 Citations (Google Scholar);
2) Marine bacterial exopolymers-mediated green synthesis of noble metal nanoparticles with antimicrobial properties, A. Scala, A. Piperno, **A.-M. Hada**, S. Astilean, A. Vulpoi, G. Ginestra, A. Marino, A. Nostro, V. Zammuto, C. Gugliandolo, **Polymers** 11 (2019) 1157-1167 (IF 3.4), 31 Citations (Google Scholar);
3) Dopamine Photochemical Behaviour under UV Irradiation, A. Falamas, A. Petran, **A.-M. Hada**, A. Bende, **International Journal Molecular Sciences** 23 (2022) 5483 (IF 5.6, AIS 1.028), 4 Citations (Google Scholar)

4) Probing polyvinylpyrrolidone-passivated graphene oxide nanoflakes as contrast agents inside tissue-like phantoms via multimodal confocal microscopy, M. Potara, S. Suarasan, A.-M. Craciun, M. Focsan, **A.-M. Hada**, S. Astilean, **Talanta** 247 (2022) 123581 (IF 6.1, AIS 0.793);
5) Supramolecular assembly of pentamidine and polymeric cyclodextrin bimetallic core–shell nanoarchitectures, **A.-M. Hada**, N. Burduja, M. Abbate, C. Stagno, G. Caljon, L. Maes, N. Micale, M. Cordaro, A. Scala, A. Mazzaglia, A. Piperno, **Beilstein Journal of Nanotechnology** 13 (2022) 1361 (IF 3.1, AIS 0.475);
6) Controlling the optical and morphological stability of 4-mercaptobenzoic acid-modified triangular silver nanoplates in saline environments, S. Suarasan, **A.-M. Hada**, M. Muntean, A. Vulpoi, M. Potara, S. Astilean, **Applied Surface Science** 638 (2023) 158126 (IF 6.7, AIS 0.865); (first author with equal contribution)
7) Albumin nanoparticles with tunable ultraviolet-to-red autofluorescence for label-free cell imaging and selective biosensing of copper ion, R. Borlan, O. Soritau, D. Maniu, **A.-M. Hada**, A. Florea, S. Astilean, M. Focsan, **International Journal of Biological Macromolecules** 242 (2023) 125129 (IF 8.2, AIS 0.918);

Conference attendings

Oral presentations

1) Investigation of protein-stabilized gold nanoclusters with applicability in cellular imaging, **A.-M. Hada**, A.-M. Craciun, M. Focsan, O. Soritau, S. Astilean, **National Conference of Physics' PhD students 2020**, Iasi, Romania;

2) Novel paper-based sensing platform using photoluminescent gold nanoclusters for easy, sensitive and selective naked-eye detection of Cu^{2+}, **A.-M. Hada**, M. Zetes, M. Focsan, T. Nagy-Simon, A. M. Craciun, **Nanotexnology 2021**, Thessaloniki, Greece;

Poster presentations

1) Novel paper-based sensing platform using photoluminescent gold nanoclusters for easy, sensitive and selective naked-eye detection of Cu^{2+}, **A.-M. Hada**, M. Zetes, M. Focsan, T.

Nagy-Simon, A. M. Craciun, **International Summer School on Nanosciences & Nanotechnologies, Organic Electronics & Nanomedicine 2021**, Thessaloniki, Greece;

2) Colorimetric detection of C-reactive protein using aptamer-modified gold-silver core-shell nanoparticles, A.-M. Hada, T. Nagy-Simon, S. Suarasan, S. Astilean, M. Potara, **The 15th International Conference on Physics of Advanced Materials (ICPAM-15) 2021,** Sant Feliu de Guixols, Spain;

3) Intrisic photoluminescent protein-stabilized gold nanoclusters: towards fluorescence imaging applications, A.-M. Hada, A.-M. Craciun, M. Focsan, O. Soritau, S. Astilean, **The 15th International Conference on Physics of Advanced Materials (ICPAM-15),** Sant Feliu de Guixols, Spain;

4) Highly-sensitive C-reactive protein detection based on the selective aggregation of aptamer-conjugated silver nanoparticles, **A.-M. Hada**, S. Suarasan, T. Nagy-Simon, A. Vulpoi, S. Astilean, M. Potara, **The 7th Nanoinnovation 2022**, Rome, Italy;

5) Cationic Cyclodextrin Polymer vs Chitosan for SERS-nanoTags fabrication, **A.-M. Hada**, M. Potara, S. Astilean, A. Cordaro, G. Neri, M. Malanga, A. Mazzaglia, A. Scala, A. Piperno, **20th International Cyclodextrin Symposium (20th ICS) 2022**, Giardini Naxos, Italy;

6) Aptamer-functionalized gold nanoparticles for the highly-sensitive dual-detection of C-reactive protein, **A.-M. Hada**, S. Suarasan, V. Moldovan, S. Astilean, M. Potara, **Molecular Plasmonics 2023**, Jena, Germany;

Conference contributions

1) Aptamer-modified citrate-capped gold nanoparticles for sensitive visual detection of C-reactive Protein, V.-A. Moldovan, A.-M. Hada, S. Suarasan, T. Nagy-Simon, A. Vulpoi, S. Astilean, M. Potara, **The 6th International Conference of Analytical and**

Nanoanalytical Methods for Biomedical and Environmental Sciences (IC-ANMBES 2022), Brasov, Romania – poster presentation;

2) Synthesis and characterization of novel histidine-stabilized gold nanoclusters for the sensitive and selective detection of Fe from water samples, M. Zetes, **A.-M. Hada**, M. Focsan, S. Astilean, A.-M. Craciun, **The 6th International Conference on Analytical and Nanoanalytical Methods for Biomedical and Environmental Sciences (IC-ANMBES 2022)**, Brasov, Romania – poster presentation (Best Poster Presentation Award);

3) Colorimetric and thermoplasmonic dual-mode detection of C-reactive protein based on aptamer conjugated gold nanoparticles, S. Suarasan, **A.-M. Hada**, V.-A. Moldovan, S. Astilean, M. Potara, **The 6th International Conference on Materials: Advanced and Emerging Materials (ICM 2022)**, Barcelona, Spain – poster presentation

4) Portable paper sensing platform using novel histidine-stabilized gold nanoclusters for fast naked-eye detection of Fe ions from water, M. Zetes, A.-M. Hada, M. Focsan, S. Astilean, A.-M. Craciun, **The 9th IUPAC International Conference on Green Chemistry 2022**, Athene, Greece – poster presentation;

Awards

- ✓ CYCLONET ACRI Young Investigator Training Program 2019 AWARD – Associazione Casse di Risparmio Italiane - 3000 € prize to research at least 1 month in an Italian laboratory. I chose to do my mobility in Prof. Anna Piperno's research team from CHIBIOFARAM Department, University of Messina, with whom I had and continue to have a multidisciplinary collaboration which resulted in two publications and one poster presentation and probably many more to come.

Teaching activity

- ✓ I taught the laboratories and seminars for the “Metode spectroscopice de analiza” course at the Biology and Geology Faculty from Babes-Bolyai University for one semester.

Specialization courses

- ✓ Participated at the 18th International Course in Principles and Applications of Time-resolved Fluorescence Spectroscopy 2021

Funding and grants

During my PhD I was a member in 3 National Research project, and I would like to thank UEFISCDI for the financial support and the research projects’ directors for giving me the opportunity to work in their projects in which I had the following positions:

1) Research Assistant in the Romanian National Research Project called "New targeted optical imaging nanoprobes for near-infrared (NIR) real-time (RT) image-guided surgery of ovarian cancer”, project code: PN-III-P4-IDPCCF-2016-0142;
2) Research Assistant in the Romanian National Research Project called "Direct, sensitive and selective fluorescence “turn-off” detection of metallic contaminants from water using photoluminescent gold nanoclusters”, project code: PN-III-P1-1.1-TE-2019-0700;
3) Research Assistant in the Romanian National Research Project called “Designing new plasmonic aptasensors for detection and monitoring of infections”, project code: PN-III-P4-ID-PCE-2020-1592;

I also won a national scholarship in my last year of PhD, the POCU 153310 - “Dezvoltarea competențelor de cercetare avansată și aplicată în logica STEAM + Health” scholarship and I would like to thank the Babes-Bolyai University for entrusting me with opportunity and for the financial support.

References

[1] L. Liu, A. Corma, Metal Catalysts for Heterogeneous Catalysis: From Single Atoms to Nanoclusters and Nanoparticles, Chem. Rev. 118 (2018) 4981–5079. https://doi.org/10.1021/acs.chemrev.7b00776.

[2] M.A. Garcia, Surface plasmons in metallic nanoparticles: fundamentals and applications, J. Phys. D: Appl. Phys. 44 (2011) 283001. https://doi.org/10.1088/0022-3727/44/28/283001.

[3] J. Xie, Y. Zheng, J.Y. Ying, Protein-Directed Synthesis of Highly Fluorescent Gold Nanoclusters, J. Am. Chem. Soc. 131 (2009) 888–889. https://doi.org/10.1021/ja806804u.

[4] D.-Y. Fu, Y.-R. Xue, Y. Guo, Z. Qu, H.-W. Li, H. Wu, Y. Wu, Strong red-emitting gold nanoclusters protected by glutathione *S* -transferase, Nanoscale. 10 (2018) 23141–23148. https://doi.org/10.1039/C8NR05691A.

[5] H. Pezhhan, M. Akhond, M. Shamsipur, Histidine capped-gold nanoclusters mediated fluorescence detection of glucose and hydrogen peroxide based on glucose oxidase-mimicking property of gold nanoparticles via an inner filter effect mechanism, Journal of Luminescence. 228 (2020) 117604. https://doi.org/10.1016/j.jlumin.2020.117604.

[6] R.J. Giguere, T.L. Bray, S.M. Duncan, G. Majetich, Application of commercial microwave ovens to organic synthesis., Tetrahedron Letters. 27 (1986) 4945–4948. https://doi.org/10.1016/S0040-4039(00)85103-5.

[7] R. Gedye, F. Smith, K. Westaway, H. Ali, L. Baldisera, L. Laberge, J. Rousell, The use of microwave ovens for rapid organic synthesis, Tetrahedron Letters. 27 (1986) 279–282. https://doi.org/10.1016/S0040-4039(00)83996-9.

[8] H. Cui, Z.-S. Shao, Z. Song, Y.-B. Wang, H.-S. Wang, Development of gold nanoclusters: from preparation to applications in the field of biomedicine, J. Mater. Chem. C. 8 (2020) 14312–14333. https://doi.org/10.1039/D0TC03443F.

[9] A.P. Alivisatos, Semiconductor Clusters, Nanocrystals, and Quantum Dots, Science. 271 (1996) 933–937. https://doi.org/10.1126/science.271.5251.933.

[10] M. Azharuddin, G.H. Zhu, D. Das, E. Ozgur, L. Uzun, A.P.F. Turner, H.K. Patra, A repertoire of biomedical applications of noble metal nanoparticles, Chem. Commun. 55 (2019) 6964–6996. https://doi.org/10.1039/C9CC01741K.

[11] K.S. Siddiqi, A. Husen, R.A.K. Rao, A review on biosynthesis of silver nanoparticles and their biocidal properties, J Nanobiotechnol. 16 (2018) 14. https://doi.org/10.1186/s12951-018-0334-5.

[12] Y. Tang, X. Zeng, J. Liang, Surface Plasmon Resonance: An Introduction to a Surface Spectroscopy Technique, J. Chem. Educ. 87 (2010) 742–746. https://doi.org/10.1021/ed100186y.

[13] Y. Liu, E. Naumenko, F. Akhatova, Q. Zou, R. Fakhrullin, X. Yan, Self-assembled peptide nanoparticles for enhanced dark-field hyperspectral imaging at the cellular and invertebrate level, Chemical Engineering Journal. 424 (2021) 130348. https://doi.org/10.1016/j.cej.2021.130348.

[14] A.-M. Hada, M. Potara, S. Suarasan, A. Vulpoi, T. Nagy-Simon, E. Licarete, S. Astilean, Fabrication of gold–silver core–shell nanoparticles for performing as ultrabright SERS-nanotags inside human ovarian cancer cells, Nanotechnology. 30 (2019) 315701. https://doi.org/10.1088/1361-6528/ab1857.

[15] X. He, K. Wang, Z. Cheng, *In vivo* near-infrared fluorescence imaging of cancer with nanoparticle-based probes: *In vivo* near-infrared fluorescence imaging, WIREs Nanomed Nanobiotechnol. 2 (2010) 349–366. https://doi.org/10.1002/wnan.85.

[16] E. Dimitrow, I. Riemann, A. Ehlers, M.J. Koehler, J. Norgauer, P. Elsner, K. König, M. Kaatz, Spectral fluorescence lifetime detection and selective melanin imaging by multiphoton laser tomography for melanoma diagnosis, Experimental Dermatology. 18 (2009) 509–515. https://doi.org/10.1111/j.1600-0625.2008.00815.x.

[17] Z. Jin, D. Geißler, X. Qiu, K.D. Wegner, N. Hildebrandt, A Rapid, Amplification-Free, and Sensitive Diagnostic Assay for Single-Step Multiplexed Fluorescence Detection of MicroRNA, Angew. Chem. Int. Ed. 54 (2015) 10024–10029. https://doi.org/10.1002/anie.201504887.

[18] X. Du, W. Wang, C. Wu, B. Jia, W. Li, L. Qiu, P. Jiang, J. Wang, Y.-Q. Li, Enzyme-responsive turn-on nanoprobes for *in situ* fluorescence imaging and localized photothermal treatment of multidrug-resistant bacterial infections, J. Mater. Chem. B. (2020) 10.1039.D0TB00750A. https://doi.org/10.1039/D0TB00750A.

[19] H. Kobayashi, M. Ogawa, R. Alford, P.L. Choyke, Y. Urano, New Strategies for Fluorescent Probe Design in Medical Diagnostic Imaging, Chem. Rev. 110 (2010) 2620–2640. https://doi.org/10.1021/cr900263j.

[20] A. Ramanathan, P.K. Agarwal, Evolutionarily Conserved Linkage between Enzyme Fold, Flexibility, and Catalysis, PLoS Biol. 9 (2011) e1001193. https://doi.org/10.1371/journal.pbio.1001193.

[21] X. Michalet, S. Weiss, M. Jäger, Single-Molecule Fluorescence Studies of Protein Folding and Conformational Dynamics, Chem. Rev. 106 (2006) 1785–1813. https://doi.org/10.1021/cr0404343.

[22] S. Achilefu, R.B. Dorshow, J.E. Bugaj, R. Rajagopalan, Novel Receptor-Targeted Fluorescent Contrast Agents for In Vivo Tumor Imaging:, Investigative Radiology. 35 (2000) 479–485. https://doi.org/10.1097/00004424-200008000-00004.

[23] S. Zaiba, F. Lerouge, A.-M. Gabudean, M. Focsan, J. Lermé, T. Gallavardin, O. Maury, C. Andraud, S. Parola, P.L. Baldeck, Transparent Plasmonic Nanocontainers Protect Organic Fluorophores against Photobleaching, Nano Lett. 11 (2011) 2043–2047. https://doi.org/10.1021/nl2004847.

[24] M. Monici, Cell and tissue autofluorescence research and diagnostic applications, in: Biotechnology Annual Review, Elsevier, 2005: pp. 227–256. https://doi.org/10.1016/S1387-2656(05)11007-2.

[25] L. Zhou, Q. Wang, Y. Tan, M.J. Lang, H. Sun, X. Liu, Rational Development of Near-Infrared Fluorophores with Large Stokes Shifts, Bright One-Photon, and Two-Photon Emissions for Bioimaging and Biosensing Applications, Chem. Eur. J. 23 (2017) 8736–8740. https://doi.org/10.1002/chem.201701365.

[26] A.-M. Hada, A.-M. Craciun, M. Focsan, R. Borlan, O. Soritau, M. Todea, S. Astilean, Folic acid functionalized gold nanoclusters for enabling targeted fluorescence imaging of human ovarian cancer cells, Talanta. 225 (2021) 121960. https://doi.org/10.1016/j.talanta.2020.121960.

[27] A.-M. Hada, A.-M. Craciun, S. Astilean, Gold nanoclusters performing as contrast agents for non-invasive imaging of tissue-like phantoms *via* two-photon excited fluorescence lifetime imaging, Analyst. 146 (2021) 7126–7130. https://doi.org/10.1039/D1AN01394G.

[28] J.C. Widen, M. Tholen, J.J. Yim, M. Bogyo, Methods for analysis of near-infrared (NIR) quenched-fluorescent contrast agents in mouse models of cancer, in: Methods in Enzymology, Elsevier, 2020: pp. 141–166. https://doi.org/10.1016/bs.mie.2020.04.012.

[29] K. Purich, J.T. Dang, A. Poonja, W.Y.L. Sun, D. Bigam, D. Birch, S. Karmali, Intraoperative fluorescence imaging with indocyanine green in hepatic resection for malignancy: a systematic review and meta-analysis of diagnostic test accuracy studies, Surg Endosc. 34 (2020) 2891–2903. https://doi.org/10.1007/s00464-020-07543-2.

[30] C. Zhang, D. Jiang, B. Huang, C. Wang, L. Zhao, X. Xie, Z. Zhang, K. Wang, J. Tian, Y. Luo, Methylene Blue–Based Near-Infrared Fluorescence Imaging for Breast Cancer Visualization in Resected Human Tissues, Technol Cancer Res Treat. 18 (2019) 153303381989433. https://doi.org/10.1177/1533033819894331.

[31] J. Liu, P.N. Duchesne, M. Yu, X. Jiang, X. Ning, R.D. Vinluan, P. Zhang, J. Zheng, Luminescent Gold Nanoparticles with Size-Independent Emission, Angew. Chem. Int. Ed. 55 (2016) 8894–8898. https://doi.org/10.1002/anie.201602795.

[32] A.-M. Hada, A.-M. Craciun, M. Focsan, A. Vulpoi, E.-L. Borcan, S. Astilean, Glutathione-capped gold nanoclusters as near-infrared-emitting efficient contrast agents for confocal fluorescence imaging of tissue-mimicking phantoms, Microchim Acta. 189 (2022) 337. https://doi.org/10.1007/s00604-022-05440-0.

[33] J.-J. Li, D. Qiao, J. Zhao, G.-J. Weng, J. Zhu, J.-W. Zhao, Ratiometric fluorescence detection of Hg^{2+} and Fe^{3+} based on BSA-protected Au/Ag nanoclusters and His-stabilized Au nanoclusters, Methods Appl. Fluoresc. 7 (2019) 045001. https://doi.org/10.1088/2050-6120/ab34be.

[34] R. Dai, W. Deng, P. Hu, C. You, L. Yang, X. Jiang, X. Xiong, K. Huang, One-pot synthesis of bovine serum albumin protected gold/silver bimetallic nanoclusters for ratiometric and visual

detection of mercury, Microchemical Journal. 139 (2018) 1–8. https://doi.org/10.1016/j.microc.2018.02.010.

[35] Y. Qi, J. Zhao, G. Weng, J. Li, J. Zhu, J. Zhao, Modification-free colorimetric and visual detection of Hg2+ based on the etching from core-shell structural Au-Ag nanorods to nanorices, Sensors and Actuators B: Chemical. 267 (2018) 181–190. https://doi.org/10.1016/j.snb.2018.04.042.

[36] P. Ferenci, T. Litwin, J. Seniow, A. Czlonkowska, Encephalopathy in Wilson Disease: Copper Toxicity or Liver Failure?, Journal of Clinical and Experimental Hepatology. 5 (2015) S88–S95. https://doi.org/10.1016/j.jceh.2014.09.002.

[37] N. Malhotra, T.-R. Ger, B. Uapipatanakul, J.-C. Huang, K.H.-C. Chen, C.-D. Hsiao, Review of Copper and Copper Nanoparticle Toxicity in Fish, Nanomaterials. 10 (2020) 1126. https://doi.org/10.3390/nano10061126.

[38] M. Zheng, H. Tan, Z. Xie, L. Zhang, X. Jing, Z. Sun, Fast Response and High Sensitivity Europium Metal Organic Framework Fluorescent Probe with Chelating Terpyridine Sites for Fe^{3+}, ACS Appl. Mater. Interfaces. 5 (2013) 1078–1083. https://doi.org/10.1021/am302862k.

[39] E.V. Salnikova, T.I. Burtseva, M.G. Skalnaya, A.V. Skalny, A.A. Tinkov, Copper and zinc levels in soil, water, wheat, and hair of inhabitants of three areas of the Orenburg region, Russia, Environmental Research. 166 (2018) 158–166. https://doi.org/10.1016/j.envres.2018.05.028.

[40] C. Song, B. Yang, Y. Yang, L. Wang, SERS-based mercury ion detections: principles, strategies and recent advances, Sci. China Chem. 59 (2016) 16–29. https://doi.org/10.1007/s11426-015-5504-9.

[41] F.-Y. Yang, S.-J. Jiang, A.C. Sahayam, Combined use of HPLC–ICP-MS and microwave-assisted extraction for the determination of cobalt compounds in nutritive supplements, Food Chemistry. 147 (2014) 215–219. https://doi.org/10.1016/j.foodchem.2013.09.141.

[42] C.M.G. Van Den Berg, Chemical Speciation of Iron in Seawater by Cathodic Stripping Voltammetry with Dihydroxynaphthalene, Anal. Chem. 78 (2006) 156–163. https://doi.org/10.1021/ac051441+.

[43] G.L. Arnold, S. Weyer, A.D. Anbar, Fe Isotope Variations in Natural Materials Measured Using High Mass Resolution Multiple Collector ICPMS, Anal. Chem. 76 (2004) 322–327. https://doi.org/10.1021/ac034601v.

[44] A.-M. Hada, M. Zetes, M. Focsan, S. Astilean, A.-M. Craciun, Photoluminescent Histidine-Stabilized Gold Nanoclusters as Efficient Sensors for Fast and Easy Visual Detection of Fe Ions in Water Using Paper-Based Portable Platform, IJMS. 23 (2022) 12410. https://doi.org/10.3390/ijms232012410.

[45] A.-M. Hada, M. Zetes, M. Focsan, T. Nagy-Simon, A.-M. Craciun, Novel paper-based sensing platform using photoluminescent gold nanoclusters for easy, sensitive and selective naked-

eye detection of Cu2+, Journal of Molecular Structure. 1244 (2021) 130990. https://doi.org/10.1016/j.molstruc.2021.130990.

[46] A. Gundogdu, Acute toxicity of zinc and copper for rainbow trout (Onchorhyncus mykiss), JFS.Com. (2008). https://doi.org/10.3153/jfscom.2008039.

[47] Y. Su, L. Qi, X. Mu, M. Wang, A fluorescent probe for sensing ferric ions in bean sprouts based on L -histidine-stabilized gold nanoclusters, Anal. Methods. 7 (2015) 684–689. https://doi.org/10.1039/C4AY02186J.

[48] Q. Zhao, S. Chen, L. Zhang, H. Huang, Y. Zeng, F. Liu, Multiplex sensor for detection of different metal ions based on on–off of fluorescent gold nanoclusters, Analytica Chimica Acta. 852 (2014) 236–243. https://doi.org/10.1016/j.aca.2014.09.029.

[49] World Health Organization, International Programme on Chemical Safety, Guidelines for drinking-water quality. Vol. 2, Health criteria and other supporting information, (1996). https://apps.who.int/iris/handle/10665/38551.

[50] N. Arora, A. Mehta, A. Mishra, S. Basu, 4-Nitrophenol reduction catalysed by Au-Ag bimetallic nanoparticles supported on LDH: Homogeneous vs. heterogeneous catalysis, Applied Clay Science. 151 (2018) 1–9. https://doi.org/10.1016/j.clay.2017.10.015.

[51] G. Barbillon, Latest Novelties on Plasmonic and Non-Plasmonic Nanomaterials for SERS Sensing, Nanomaterials. 10 (2020) 1200. https://doi.org/10.3390/nano10061200.

[52] P. Bhatia, S.S. Verma, M.M. Sinha, Magneto-plasmonic Co@M (M = Au/Ag/Au-Ag) core-shell nanoparticles for biological imaging and therapeutics, Journal of Quantitative Spectroscopy and Radiative Transfer. 251 (2020) 107095. https://doi.org/10.1016/j.jqsrt.2020.107095.

[53] V. Prabhawathi, P.M. Sivakumar, T. Boobalan, C.M. Manohar, M. Doble, Design of antimicrobial polycaprolactam nanocomposite by immobilizing subtilisin conjugated Au/Ag core-shell nanoparticles for biomedical applications, Materials Science and Engineering: C. 94 (2019) 656–665. https://doi.org/10.1016/j.msec.2018.10.020.

[54] S. Zhou, M. Zhao, T.-H. Yang, Y. Xia, Decahedral nanocrystals of noble metals: Synthesis, characterization, and applications, Materials Today. 22 (2019) 108–131. https://doi.org/10.1016/j.mattod.2018.04.003.

[55] R. Kotha, G. Fernandes, A.N. Nikam, S. Kulkarni, A. Pandey, S. Pandey, S. Mutalik, Surface engineered bimetallic nanoparticles based therapeutic and imaging platform: recent advancements and future perspective, Materials Science and Technology. 36 (2020) 1729–1748. https://doi.org/10.1080/02670836.2020.1832323.

[56] A. Scala, G. Neri, N. Micale, M. Cordaro, A. Piperno, State of the Art on Green Route Synthesis of Gold/Silver Bimetallic Nanoparticles, Molecules. 27 (2022) 1134. https://doi.org/10.3390/molecules27031134.

[57] G. Sharma, A. Kumar, S. Sharma, Mu. Naushad, R. Prakash Dwivedi, Z.A. ALOthman, G.T. Mola, Novel development of nanoparticles to bimetallic nanoparticles and their composites:

A review, Journal of King Saud University - Science. 31 (2019) 257–269. https://doi.org/10.1016/j.jksus.2017.06.012.

[58] K. Loza, M. Heggen, M. Epple, Synthesis, Structure, Properties, and Applications of Bimetallic Nanoparticles of Noble Metals, Adv. Funct. Mater. 30 (2020) 1909260. https://doi.org/10.1002/adfm.201909260.

[59] A.-M. Hada, M. Potara, S. Astilean, A. Cordaro, G. Neri, M. Malanga, A. Nostro, A. Mazzaglia, A. Scala, A. Piperno, Linezolid nanoAntiobiotics and SERS-nanoTags based on polymeric cyclodextrin bimetallic core-shell nanoarchitectures, Carbohydrate Polymers. 293 (2022) 119736. https://doi.org/10.1016/j.carbpol.2022.119736.

[60] C. Foti, A. Piperno, A. Scala, O. Giuffrè, Oxazolidinone Antibiotics: Chemical, Biological and Analytical Aspects, Molecules. 26 (2021) 4280. https://doi.org/10.3390/molecules26144280.

[61] W. Ansar, S. Ghosh, C-reactive protein and the biology of disease, Immunol Res. 56 (2013) 131–142. https://doi.org/10.1007/s12026-013-8384-0.

[62] B. Clyne, J.S. Olshaker, The C-reactive protein, The Journal of Emergency Medicine. 17 (1999) 1019–1025. https://doi.org/10.1016/S0736-4679(99)00135-3.

[63] T.A. Pearson, G.A. Mensah, R.W. Alexander, J.L. Anderson, R.O. Cannon, M. Criqui, Y.Y. Fadl, S.P. Fortmann, Y. Hong, G.L. Myers, N. Rifai, S.C. Smith, K. Taubert, R.P. Tracy, F. Vinicor, Markers of Inflammation and Cardiovascular Disease, Circulation. 107 (2003) 499–511. https://doi.org/10.1161/01.CIR.0000052939.59093.45.